Missing Information Reconstruction of Remote Sensing Data: A Technical Review

Huanfeng Shen, *Senior Member, IEEE*, Xinghua Li, *Graduate Student Member, IEEE*, Qing Cheng, Chao Zeng, Gang Yang, Huifang Li, *Member, IEEE*, Liangpei Zhang, *Senior Member, IEEE*

***Abstract*—Because of sensor malfunction and poor atmospheric conditions, there is usually a great deal of missing information in optical remote sensing data, which reduces the usage rate and hinders the follow-up interpretation. In the past decades, missing information reconstruction of remote sensing data has become an active research field, and a large number of algorithms have been developed. However, to the best of our knowledge, there has not, to date, been a study that has been aimed at expatiating and summarizing the current situation. This is therefore our motivation in this review. This paper provides an introduction to the principles and theories of missing information reconstruction of remote sensing data. We classify the established and emerging algorithms into four main categories, followed by a comprehensive comparison of them from both experimental and theoretical perspectives. This paper also predicts the promising future research directions.**

I. Introduction

Remote sensing instruments can capture information about the atmosphere, ocean, and the earth's surface. They are one of the most frequently used and most powerful approaches to understanding and investigating our planet. However, because of defective sensors and poor atmospheric conditions (e.g., thick clouds), the acquired remote sensing data are often so incomplete (we also say that they have missing information) that the data usability is greatly reduced.

For example, 15 of the 20 detectors in the Aqua Moderate Resolution Imaging Spectroradiometer (MODIS) band 6 are ineffective [1]; the scan line corrector (SLC) of the Landsat enhanced thematic mapper plus (ETM+) sensor has permanently failed [2]; and the ozone monitoring instrument (OMI) onboard the Aura satellite is subject to a row anomaly problem. On average, at any one time, approximately 35% of the global land surface is obscured by clouds [3], and in an individual country, the rate of cloud cover can be much higher, e.g., in Canada, from 50% to 80% of the earth's surface is covered by clouds in mid-morning [4]. Since cloud cover is frequently inevitable in the observation process, passive remote sensing data contain lots of missing information. Clouds in remote sensing data are useful information for liquid water research; however, in this paper, they are considered as useless information that obstructs the observation. It is noteworthy that only passive remote sensing imageries are affected by atmospheric conditions; thus, when it comes to the atmosphere (or clouds) in the following descriptions, the data are from passive sensor platforms.

Dead pixels resulting from sensor failure or random error are also a common phenomenon. Missing information limits the regular and further applications of remote sensing data, e.g. classification [5], unmixing, target detection, etc. As a result, reconstructing the missing information of remote sensing data is of great significance for many practical applications (e.g., improving the subsequent interpretation accuracy and enhancing the data availability).

In order to intuitively perceive the information loss of remote sensing data, we show some concrete examples in Fig. 1. In short, Fig. 1(a)–(c) are the consequences of sensor failure, and Fig. 1(d)–(f) are the consequences of cloud obscuration. The figures include digital number (DN) value images and quantitative products of remote sensing, i.e., reflectance, land surface temperature (LST), the normalized difference vegetation index (NDVI), and ozone.

In our opinion, according to the different sources of the complementary information when reconstructing the missing information, the present algorithms can be primarily classified into four categories: 1) spatial-based methods, without any other auxiliary information source; 2) spectral-based methods, which extract the complementary information from other spectra; 3) temporal-based methods, which extract the complementary information from other data acquired at the same position and at different time periods (hereafter, we say they are multitemporal); and 4) hybrid methods, which extract the complementary information by a combination of the three previous approaches.

We believe that this paper will not only contribute to a summarization of the current situation of reconstruction algorithms for the missing information of remote sensing data, but will also point out the promising research and development

Manuscript received September 29, 2014; revised April 16, 2015; accepted April 23, 2015. This work was supported by the National Natural Science Foundation of China (NSFC) under Grant Nos. 41271376 and 41422108, the Program for Changjiang Scholars and Innovative Research Team in University under Grant No. IRT1278.

Huanfeng Shen, Xinghua Li, Gang Yang and Huifang Li are with the School of Resource and Environmental Sciences, Wuhan University, P.R. China (e-mail: shenhf@whu.edu.cn, lixinghua5540@whu.edu.cn, love64080@163.com, huifangli@whu.edu.cn).

Qing Cheng and Liangpei Zhang are with the State Key Laboratory of Information Engineering in Surveying, Mapping, and Remote Sensing, Wuhan University, P.R. China (e-mail: qingcheng@whu.edu.cn, zlp62@whu.edu.cn).

Chao Zeng is with the State Key Laboratory of Information Engineering in Surveying, Mapping, and Remote Sensing, Wuhan University, P.R. China, and the Department of Hydraulic Engineering, Tsinghua University, Beijing, China (E-mail: zengchaozc@hotmail.com).

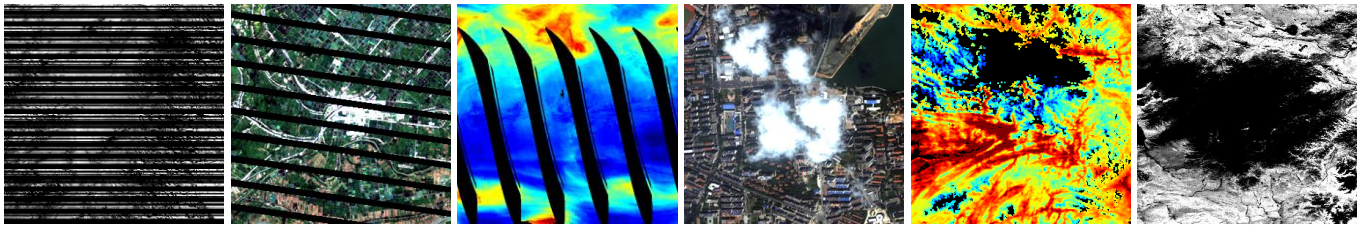

(a) (b) (c) (d) (e) (f)

Fig. 1. Several examples of remote sensing data with missing information. In addition to the white clouds, the dark regions also represent missing information. (a) Reflectance of Aqua MODIS band 6 with sensor failure. (b) DN value of Landsat ETM+ with the SLC-off problem. (c) Ozone of Aura OMI with the row anomaly problem. (d) DN value of IKONOS-2 with cloud obscuration. (e) LST of MODIS with cloud obscuration. (f) NDVI of MODIS with cloud obscuration. Note that the dynamic range [−1, 1] is stretched linearly to [0, 255] for the visual effect.

directions in the future. The ultimate objective will be beneficial to the subsequent applications of remote sensing data.

The rest of this review is organized as follows. In Section II, we make a brief description of what is entailed in the missing information reconstruction of remote sensing data. Sections III–VI survey the algorithms used to reconstruct the missing information of remote sensing data, based on the four kinds of methods, respectively, and also provide the experimental comparisons. Finally, the conclusion and prospects are presented in Section VIII.

II. Problem Description

Remote sensing data with missing information may be two-dimensional (2D) (e.g., panchromatic images and some quantitative data), three-dimensional (3D) (e.g., multi/hyper-spectral images), or four-dimensional (4D) (e.g., multitemporal 3D data). In other words, the data have various forms. On the other hand, reconstructing the missing information of remote sensing data is an ill-posed inverse problem. For the convenience and uniformity of the subsequent descriptions, it will be necessary to make a universal introduction to the problem. In this section, the issue of the reconstruction of remote sensing data is generally described, and the notations and symbols are explained. In this paper, vectors and matrices are denoted by bold and non-italic characters, and the scalar variables are denoted by italic and non-bold characters.

In fact, to reconstruct the missing information of remote sensing data is an issue that estimates the missing values according to the existing/remaining and valid values. For brevity, we first take the case of the simplest 2D remote sensing data as an example. As shown in Fig. 2, given 2D data $\mathbf{I}\in\mathbb{R}^{m\times n}$ ($\mathbf{I}:\boldsymbol{\Omega}\in\mathbb{R}^2\to\mathbb{R}^2$), where $\boldsymbol{\Omega}$ represents the spatial domain, it is composed of $m\times n$ points $\{p_{\mathbf{x}}\}$, and $\mathbf{x}$ is the coordinates of point $p_{\mathbf{x}}$, which is defined as $\mathbf{x}=(x,y)$. Correspondingly, $\mathbf{I}(\mathbf{x})$ represents the value of point $p_{\mathbf{x}}$. We assume that the domain $\boldsymbol{\Omega}$ is composed of missing region $\mathbf{S}$ and existing region $\mathbf{E}$, i.e., $\boldsymbol{\Omega}=\mathbf{S}\cup\mathbf{E}$ and $\mathbf{S}\cap\mathbf{E}=\varnothing$. In practice, we let $\mathbf{J}$ be the observed version of the ideal $\mathbf{I}$, which is subject to missing information, and $\mathbf{M}$ denotes the operator (mask) of the missing information, which is a diagonal matrix with diagonal elements consisting of 0 and 1, with 0 representing the missing data. In the study of reconstructing missing information, the goal is to reconstruct the value at the position $\mathbf{x}$ (in the missing region $\mathbf{S}$), based on a reasonable estimation from the existing region $\mathbf{E}$. A satisfactory result will not only be visually natural, but also in accordance with the physical meaning (mainly for remote sensing quantitative data).

As far as remote sensing data are concerned, they more usually have a 3D form, as shown in Fig. 3. In terms of the data structure, 2D remote sensing data are just a special case of 3D data, and the previously declared notations are still valid. An item of 3D remote sensing data is denoted by $\mathbf{I}\in\mathbb{R}^{m\times n\times k}$ ($\mathbf{I}:\boldsymbol{\Omega}\in\mathbb{R}^2\to\mathbb{R}^3$). Thus, the coordinates of point $p_{\mathbf{x}}$ will be defined as $\mathbf{x}=(x,y,z)$. Additionally, $\mathbf{I}^i:\boldsymbol{\Omega}\in\mathbb{R}^2\to\mathbb{R}^2$ represents the *i*-th component of $\mathbf{I}$ (the *i*-th layer in Fig. 3, from top to bottom). When some components of the multicomponent 3D remote sensing data are corrupted with missing information, and the others are intact, the intact components can provide useful information for the reconstruction of the corrupted components. This example is further discussed in Section IV.

In the field of remote sensing, items of data that are acquired

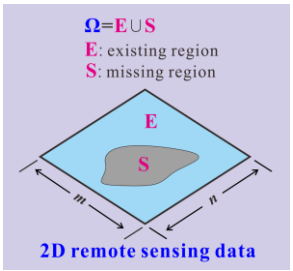

Fig. 2. Missing information of 2D remote sensing data.

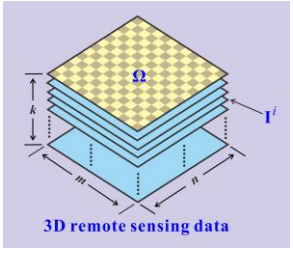

Fig. 3. 3D remote sensing data.

in the same geographical region and from different periods (multitemporal) are usually used for reconstructing missing data. Mathematically, $\{\mathbf{I}_t\}_{t=1}^{T}$ is a sequence of multitemporal remote sensing data from T different times. Without loss of any generality, $\mathbf{I}_t$ is supposed to be 3D (multicomponent) (when $k=1$, $\mathbf{I}_t$ is 2D). The previous notations are also usable; for example, $\mathbf{I}_t^i$ denotes the i-th component of the t-th remote sensing data. When a sequence of multicomponent remote sensing data is used in the reconstruction process (with maybe just a few components being used), the related data/components will reconstitute the new 3D data with a given rule (discussed in Section VI-B).

In our framework, the diverse algorithms for reconstructing the missing information of remote sensing data are divided into four main classes, based on the supplementary information sources: 1) spatial-based methods; 2) spectral-based methods; 3) temporal-based methods; and 4) hybrid methods. Note that we usually say that data with missing information are corrupted or incomplete.

III. Spatial-Based Methods

The spatial-based methods are the most traditional and most basic approach of the four kinds of methods. This category of methods fill in the missing data regions using the remaining parts of the data. This approach is based on the assumption that the missing data and the remaining data share the same statistical or geometrical structures [6]. In other words, the spatial-based methods utilize the correlations of the local or nonlocal information in the corrupted data itself. Most of these methods have been intensively studied in the field of digital image processing [7-11], and can also be applied to remote sensing image processing. The representative methods include interpolation methods [12], [13], propagated diffusion methods [7-9], [14], variation-based methods [10], [11], [15-18], and exemplar-based methods [19-21]. It should be noted that because of the lack of other reference data to judge the recovery fidelity, the goal of spatial-based reconstruction is that the recovered region shows a smooth transition at the junctions, and is as physically plausible as possible, without unconnected edges, blurring, or inconsistent texture [6].

A. Interpolation Methods

In the spatial-based reconstruction methods, interpolation algorithms are the fundamental ones. Most spatial interpolation methods can be represented as weighted averages of sampled values. They all share the same general estimation formula, as follows:

$$\hat{\mathbf{I}}(\mathbf{x}_0)=\sum_{i=1}^{N} w_i \mathbf{I}(\mathbf{x}_i) \tag{1}$$

where $\hat{\mathbf{I}}(\mathbf{x}_0)$ is the estimated value of an attribute at the point of interest $p_{\mathbf{x}_0}$, $\mathbf{I}(\mathbf{x}_i)$ is the observed value at the sampled point $p_{\mathbf{x}_i}$, w_i is the weight assigned to the sampled point $p_{\mathbf{x}_i}$, and N represents the number of sampled points used for the interpolation [22]. The most commonly used interpolation algorithms include nearest neighbor interpolation, bilinear interpolation, and cubic convolution interpolation. Geostatistical interpolation methods [13], [23] are also very useful in remote sensing data processing. Geostatistics includes several methods that use kriging algorithms for estimating intermediate values. Kriging is a kind of best linear unbiased prediction. The kriging weights are estimated by minimizing the variance σ_E^2:

$$\begin{aligned}\sigma_E^2 &= E_e\left\{\left[\mathbf{I}(\mathbf{x}_0)-\hat{\mathbf{I}}(\mathbf{x}_0)\right]^2\right\}\\ &= E_e\left[\left(\hat{\mathbf{I}}(\mathbf{x}_0)\right)^2+\left(\mathbf{I}(\mathbf{x}_0)\right)^2-2\hat{\mathbf{I}}(\mathbf{x}_0)\mathbf{I}(\mathbf{x}_0)\right]\\ &= C_e(\mathbf{x}_0,\mathbf{x}_0)-2\sum_{j=1}^{N} w_j C_e(\mathbf{x}_0,\mathbf{x}_j)+\sum_{i=1}^{N}\sum_{j=1}^{N} w_i w_j C_e(\mathbf{x}_i,\mathbf{x}_j)\end{aligned} \tag{2}$$

where $C_e(\cdot)$ is the covariance between observations, $E_e(\cdot)$ represents the expectation, w_j is the interpolation weight, and $\mathbf{x}_i$ ($\mathbf{x}_j$) is the position of point $p_{\mathbf{x}_i}$ ($p_{\mathbf{x}_j}$). A typical example of the use of an interpolation method for missing information reconstruction was described by Zhang *et al*. [12], who filled ETM+ image gaps using an ordinary kriging technique. This case study showed that the geostatistical methods can be a useful tool for interpolating missing pixels.

In general, the interpolation methods are efficient and easy to operate. However, the spatial information is not fully utilized in most interpolation methods. Therefore, these methods only work well in cases with relatively simple ground features.

B. Propagated Diffusion Methods

The propagated diffusion methods aim to recover the missing areas in such a way as to propagate the local information from the exterior to the interior of the missing areas, which is analogous to the physical phenomenon of heat propagation in physical structures. This effect can be formalized with partial differential equations (PDEs); therefore, the diffusion inpainting is performed using PDEs [24]. The simplest linear diffusion equation at time t_0 is:

$$\frac{\partial \mathbf{I}}{\partial t_0}=\Delta\mathbf{I} \tag{3}$$

where $\mathbf{I}$ represents the image data, and $\Delta\mathbf{I}$ denotes the image Laplacian. The diffusion processing at point $p_{\mathbf{x}}$ at time t_0+1 has the discrete form:

$$\overset{t_0+1}{\mathbf{I}}(\mathbf{x})=\overset{t_0}{\mathbf{I}}(\mathbf{x})+\Delta\overset{t_0}{\mathbf{I}}(\mathbf{x}) \tag{4}$$

This PDE evolution is isotropic diffusion, which propagates the image variations in all directions, as a low-pass linear filtering. For this reason, this diffusion method introduces a lot of blurring to the recovered region.

Many anisotropic PDE models, which limit the diffusion around specific directions such as edges, have been proposed for image inpainting. The diffusion inpainting method was first proposed by Bertalmio *et al*. [7] in 2000. This approach uses an anisotropic PDE model that propagates the image Laplacians

from the surrounding neighborhood into the interior of the missing area. The directions of the propagation are the directions of the isophotes, which are lines of constant intensity within an image, and they are estimated by the perpendicular direction to the image gradient at each point. The diffusion at point $p_{\mathbf{x}}$ at time t_0+1 is governed by the equation:

$$\overset{t_0+1}{\mathbf{I}}(\mathbf{x}) = \overset{t_0}{\mathbf{I}}(\mathbf{x}) + \nabla\left(\Delta \overset{t_0}{\mathbf{I}}(\mathbf{x})\right)\nabla^{\perp} \overset{t_0}{\mathbf{I}}(\mathbf{x}) \tag{5}$$

where ∇ is the gradient operator, and $\nabla^{\perp}$ represents the perpendicular direction of ∇ (i.e., the direction of the isophote). In this method, the image information is propagated inside the missing zone in a way that aims to preserve the isophote directions, as shown in Fig. 4(a).

The propagation directions are generally the key to the process of diffusion. In order to precisely determine the propagation directions, the method proposed in [14] employs an advanced tool called a "bandelet", which accurately calculates the geometrical flow of the image structures, as shown in Fig. 4(b), and then the values are propagated into the missing areas following the directions of the geometrical flow. The propagation at point $p_{\mathbf{x}_{i+1}}$ is implemented by the equation:

$$\mathbf{I}(\mathbf{x}_{i+1}) = \mathbf{I}(\mathbf{x}_i) + E_d(\mathbf{x}_{i+1}, \mathbf{x}_i)\mathbf{I}'(\mathbf{x}_i) \tag{6}$$

with

$$\mathbf{I}'(\mathbf{x}) = x'(\mathbf{x})\cos\theta + y'(\mathbf{x})\sin\theta \tag{7}$$

where $E_d(\mathbf{x}_{i+1}, \mathbf{x}_i)$ is the Euclidean distance between pixels $p_{\mathbf{x}_{i+1}}$ and $p_{\mathbf{x}_i}$. $\mathbf{I}(\mathbf{x}_{i+1})$ corresponds to the value of the nearest pixel that belongs to the missing areas, in the direction of the geometrical flow determined by the bandelet. $\mathbf{I}'(\mathbf{x})$ is the directional derivative of $\mathbf{I}$ with respect to the geometrical direction θ that is calculated by the bandelet transformation.

For the diffusion methods, many variants exist using different PDE models, including linear, nonlinear, isotropic [25], and anisotropic models [26], to favor the propagation in particular directions. These methods tend to prolong structures to the interior of the missing areas. Thus, they are suitable for recovering strong structures or filling small regions. However, they are not suitable for reconstructing large areas and textures, in which they lead to blurring.

C. Variation-Based Methods

Reconstructing the missing information of remote sensing data can also be seen as solving an ill-posed inverse problem. It is standard to use a regularization technique to make an inverse problem well posed. Image regularization can be formulated as a variational problem, where the image amounts to a function of the bounded variation (BV), and the solution is the minimization of a global energy function:

$$\hat{\mathbf{I}} = \arg\min_{\mathbf{I}}\left\{\|\mathbf{MI}-\mathbf{J}\|_q^q + \lambda U(\mathbf{I})\right\} \tag{8}$$

where $\mathbf{I}$ is the clear target image data, $\mathbf{J}$ is the observed corrupted data, and $\mathbf{M}$ is a mask signifying the missing data. The term $\|\mathbf{MI}-\mathbf{J}\|_q^q$ is the data fidelity term, which expresses the fidelity between the observed corrupted data and the target data, and the term $U(\mathbf{I})$ is the regularization term, which gives a prior model of the target data. λ is the regularization parameter, which controls the tradeoff between the data fidelity and the regularization term. It is worth noting that the regularization term ensures the uniqueness of the recovery solution; therefore, how to select an appropriate regularization is very significant. Some frequently used regularizations are introduced in the following.

1) ℓ^2 Norm Regularization: ℓ^2 norm regularizations, such as Laplacian regularization [27], Tikhonov regularization [28], and Gauss-Markov regularization [29], are the most common regularization models for image processing, because they are simple and can be solved quickly and easily. One of the representative ℓ^2 norm regularizations is Laplacian regularization, which is defined as follows:

$$U(\mathbf{I}) = \sum_{\mathbf{x}} \|\Delta\mathbf{I}(\mathbf{x})\|_2^2 \tag{9}$$

The goal of Laplacian regularization is to minimize the energy of the high-frequency component of the images; therefore, this model is able to suppress the high-frequency information and impose smoothness constraints on the images. For this reason, the Laplacian regularization inpainting model is suitable for the recovery of flat regions or for use in low-resolution images. However, it performs poorly in edge and detail information reconstruction, for which it results in blurring.

2) variation (TV) regularization, which has been widely applied for image inpainting, such as in [1]. On the basis of (8), the TV regularization can be expressed as the following equation:

$$U(\mathbf{I}) = \sum_{\mathbf{x}} |\nabla\mathbf{I}(\mathbf{x})| \tag{10}$$

TV regularization is an effective inpainting technique that is capable of recovering sharp edges. However, it suffers from the problem of connectivity, which results in the recovery results being unconnected when the width of the missing gap is larger than that of the object. Several extended TV models have been further proposed to improve the edge connectivity, e.g., the curvature-driven diffusion (CDD) models [9], high-order TV [30], and spectral-spatial adaptive TV [31].

3) $\ell^1-\ell^2$ Norm Regularization: An image usually contains both flat regions and detailed regions. Thus, some studies have tried to combine the ℓ^1 and ℓ^2 norms for the regularization. The typical model is the Huber-Markov regularization, which treats images in sections with different norms. In [15], the authors proposed a variational model with a Huber-Markov regularization for the destriping and inpainting of remote sensing images. The Huber-Markov regularization is expressed as follows:

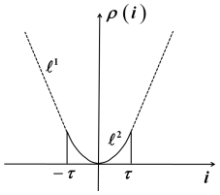

Fig. 5. Function $\rho(i)$ in Huber-Markov regularization.

(a) (b)

Fig. 4. Propagation direction and geometrical flow. (a) Propagation along isophote directions (from [7]). (b) Geometrical flow of the image structures.

$$U(\mathbf{I}) = \sum_{c \in \mathbf{C}} V_c(\mathbf{I}_\mathbf{x}) \tag{11}$$

where c is a clique within the set of all the image cliques $\mathbf{C}$, $V_c(\mathbf{I}_\mathbf{x})$ represents the potential function corresponding to the clique c, and is defined as:

$$V_c(\mathbf{I}_\mathbf{x}) = \sum_{i=1}^{4} \rho\left(d_c^i(\mathbf{I}(\mathbf{x}))\right) \tag{12}$$

where $d_c^i(\mathbf{I}(\mathbf{x}))$ is a spatial activity measure for pixel $p_\mathbf{x}$ with coordinate $\mathbf{x}$, which is formed by first- or second-order differences in the adjacent cliques of four directions (i represents the direction). $\rho(\cdot)$ is a smooth measurement function. In Huber-Markov regularization, the function $\rho(\cdot)$ is defined as:

$$\rho(i) = \begin{cases} i^2, & |i| \le \tau \\ 2\tau|i| - \tau^2, & |i| > \tau \end{cases} \tag{13}$$

where τ is a threshold parameter separating the quadratic and linear regions, as shown in Fig. 5. The smooth and detailed regions in an image can therefore be given different a priori constraints. For this reason, the Huber-Markov model can effectively suppress noise and recover the detailed information of images.

4) Nonlocal Regularization: The regularization methods mentioned above all belong to local methods that recover a pixel using the local neighboring information; therefore, they are not suitable for texture reconstruction. In recent years, the nonlocal TV regularization, which takes the nonlocal similarity within an image into consideration, has been developed for image processing, as shown in Fig. 6, and recovers a pixel using the entire image information. Cheng *et al.* [1] extended the nonlocal TV regularization to multichannel nonlocal TV regularization, and applied it to multispectral image reconstruction. On the basis of (8), the multichannel nonlocal TV regularization is as follows:

$$U(\mathbf{I}) = \sum\nolimits_{\mathbf{x}} \sqrt{\sum_{i=1}^{k} \left|\nabla_w \mathbf{I}^i(\mathbf{x})\right|^2} \tag{14}$$

where the nonlocal gradient [32] $\nabla_w \mathbf{I}(\mathbf{x}) : \mathbf{\Omega} \to \mathbf{\Omega} \times \mathbf{\Omega}$ is defined as the vector of all the partial derivatives $\nabla_w \mathbf{I}(\mathbf{x}, \cdot)$ at $\mathbf{x}$, such that:

$$(\nabla_w \mathbf{I})(\mathbf{x}, \mathbf{y}) := (\mathbf{I}(\mathbf{y}) - \mathbf{I}(\mathbf{x}))\sqrt{w(\mathbf{x}, \mathbf{y})}, \quad \forall \mathbf{y} \in \mathbf{\Omega} \tag{15}$$

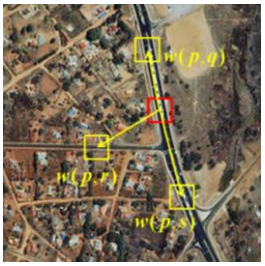

Fig. 6. Similar patches existing within an image.

where the function $w(\mathbf{x}, \mathbf{y})$ is used to compute the weight between two points $\mathbf{x}$ and $\mathbf{y}$:

$$w(\mathbf{x}, \mathbf{y}) = \exp\left\{-\frac{\left(G * \left|\mathbf{I}(\mathbf{x}+\cdot) - \mathbf{I}(\mathbf{y}+\cdot)\right|^2\right)(0)}{h^2}\right\} \tag{16}$$

where G is the Gaussian kernel, h is a filtering parameter, and $\mathbf{I}(\mathbf{x}+\cdot)$ is a patch centered at point $p_\mathbf{x}$. The nonlocal TV model is based on the idea of the nonlocal means method, and is very efficient in reducing noise while preserving the textures. The drawback is that this method is time-consuming in the process of searching for similar patches in the whole image.

Taking the image recovery as the minimization of a global energy function, the class of variation-based methods can generally achieve pleasing inpainting results, especially for the recovery of geometric structures such as edge information. However, after a few iterations, the variation-based methods tend to result in blurring, to some extent, when the missing region is large and full of complex textures.

D. Exemplar-Based Methods

The exemplar-based inpainting methods [19] are based on texture synthesis for digital images, with the aim of recovering large missing regions of texture information. The missing pixels are replaced by copying a known pixel, the neighborhood of which is the most similar to the currently available neighborhood of the input pixel to be filled. This class of inpainting methods fill the missing areas one pixel or one patch at a time in a greedy way, while maintaining coherence with nearby pixels. The simple pixel-based texture synthesis technique in [20] is performed as follows. Let $p_\mathbf{x}$ be a pixel located at the border of the missing region of an image, and $\Psi_{p_\mathbf{x}}$ is a patch centered at pixel $p_\mathbf{x}$, as shown in Fig. 7. This patch includes a known part $\Psi_{p_\mathbf{x}}^E$ and an unknown part $\Psi_{p_\mathbf{x}}^S$.

Fig. 7. Similar neighborhoods in exemplar-based methods.

The idea is to search for the patch Ψ_{p_y} (centered at p_y) that is the most similar to the known part of the input patch Ψ_{p_x}. That is to say, the central pixel p_y has a neighborhood that is the most similar to the known neighborhood of pixel p_x. The pixel p_y is then copied to recover p_x. The missing region is therefore reconstructed pixel-by-pixel by copying the known information. A problem is that this pixel-by-pixel filling algorithm suffers from a high computational cost. Patch-by-patch approaches which recover an entire patch in one step by copying an entire patch from the known region have since been proposed to reduce the computational time.

Both the pixel-based and the patch-based methods are performed in a greedy way, and the pixel or patch processing order has a strong impact on the quality of the inpainting results. Therefore, they do not ensure global image coherence. Some research work has been undertaken recently [21], [33] to progress the exemplar-based inpainting through global optimization to achieve global image coherence. In these methods, the spatial coherence is ensured via a global optimization of the Markov random field (MRF) energy function over the entire image. The patch or pixel locations are optimized in MRF by the use of belief propagation [21] or graph cuts [33].

In general, the exemplar-based inpainting methods are more suitable for filling large textured regions. These methods can achieve fine reconstruction results with a high spatial consistency and convincing visual quality. However, the fidelity and accuracy of the recovery results are usually not satisfactory.

E. Comparison of the Spatial-Based Methods

Fig. 8 shows the dead line reconstruction results with different kinds of spatial-based approaches. The original image in Fig. 8(a) is a Landsat TM image, and Fig. 8(b) is a simulated image corrupted by dead lines. From Fig. 8, it can be seen that the recovery result of the interpolation method [Fig. 8(c)] shows serious artifacts, especially in the edge of the ground features, such as the region marked with a yellow ellipse. This result indicates that when the image data contain complex terrain features or a large amount of structural information, a simple interpolation method is unsatisfactory. The result of the diffusion method [Fig. 8(d)] appears better than the interpolation method, but it introduces blurring for the

(a) (b) (c) (d) (e) (f)

Fig. 8. Experimental results for the recovery of dead lines. (a) Original image. (b) Simulated image corrupted by dead lines. Recovered images using the following: (c) Kriging interpolation in [23]; (d) BSCB diffusion method in [7]; (e) TV regularization method in [11]; and (f) Criminisi's exemplar-based method in [19].

TABLE I
PSNR AND SSIM VALUES OF THE RECOVERED IMAGES IN FIG. 8

Indicators	Corrupted image	Kriging interpolation in [23]	BSCB diffusion in [7]	TV regularization in [11]	Exemplar-based method in [19]
PSNR/dB	19.667	38.372	41.375	**41.961**	38.851
SSIM	0.73029	0.96105	0.97810	**0.98253**	0.96744

(a) (b) (c) (d) (e)

Fig. 9. Experimental results for the recovery of a cloudy image. (a) Original cloudy image. Recovered images using the following: (b) the kriging interpolation method in [23]; (c) the BSCB diffusion method in [7]; (d) the TV regularization method in [11]; and (e) Criminisi's exemplar-based method in [19].

recovery, as shown in the yellow ellipse region. The result of the variation-based method [Fig. 8(e)] appears more visually plausible than the results of the other three methods. The recovered dead lines are spatially continuous, and the sharp edges are recovered well. However, for the TV inpainting, the problem of connectivity arises, such as in the regions labeled with yellow circles in Fig. 8(e), where the white line object in the red circle region is unconnected since the missing gap is wider than the line, while it is connected in the green circle region since the missing gap in that region is narrower than the line. In the result of the exemplar-based method [Fig. 8(f)], lots of spurious detailed information appears in the dead line regions. Moreover, we can see that it is weak in curve connection, such as in the region marked with a yellow ellipse. This experiment shows that the variation-based inpainting methods are in general a good choice for the recovery of small gaps in remote sensing images.

The quantitative assessment of the four results in TABLE I also indicates the superior performance of the variation-based inpainting methods. In TABLE I, the peak signal-to-noise ratio (PSNR) and structural similarity (SSIM) [34] values of Fig. 8 are provided to give an overall quantitative evaluation. Here, it can be seen that the interpolation method (kriging interpolation) gets the worst reconstruction result, and the variation-based method (TV regularization) obtains the best reconstruction result.

Fig. 9 shows large-region reconstruction results with four kinds of spatial-based approaches. Fig. 9(a) is the original cloudy image. From the recovery results [Fig. 9(b)–(e)], it can be clearly seen that the exemplar-based method obtains a better reconstruction result than the other methods. Since the ground features are complex and the cloudy region is large, the interpolation, diffusion, and variation-based methods are not able to deal with this situation well, bringing serious blurring. However, the exemplar-based method is capable of obtaining a spatially continuous result, with more convincing visual quality. Furthermore, in the result of the exemplar-based method, the cloudy region is recovered with some ground features which are consistent with the neighbor information. Regardless of the accuracy, the exemplar-based method achieves a good result, with fine spatial continuity and more convincing visual quality.

IV. Spectral-Based Methods

Because of the absence of sufficient prior information, the spatial-based methods usually fail to reconstruct large-area missing information. In this case, in order to obtain a satisfactory effect, extracting the complementary information from the spectral domain is helpful. In multispectral and hyperspectral images, there is much redundant spectral information, due to the characteristics of the sensors. This redundant information can be used to reconstruct the missing data in a specific band. However, the premise is that the corrupted multispectral data have both incomplete (missing information) and complete spectral bands, and there must be some residual information in the corrupted band; otherwise, the spectral correlation cannot be easily made use of. The basic idea of this class of methods is to make use of the other complete spectral bands (one or more) to reconstruct the incomplete band by modeling the latent relationship between the incomplete and complete bands. We believe that the spectral correlation makes a better difference on the condition that the missing information is different in the spectral bands. For example, the missing locations are different, or one band has missing information and the other bands are complete. Such missing information problems are often caused by the sensor, where some channels are well recorded while others are not. However, the damaged band may be relevant to a particular intact band. The missing data can then be recovered by the fine band and the corresponding band relationship.

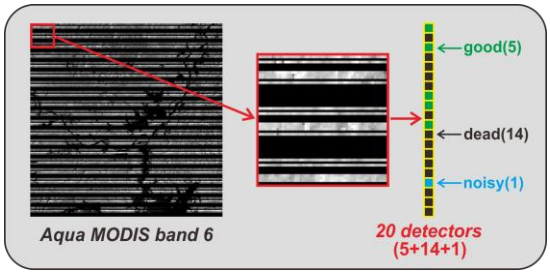

Fig. 10. Sensor failure of Aqua MODIS band 6.

To our knowledge, only a few recovery algorithms have been developed based on complementary spectral information. The typical case is the Aqua MODIS band 6 black stripe imagery. As 15 of the 20 detectors are either noisy or non-functional, there are periodic along-scan stripes of missing data covering the entire image, as shown in Fig. 10. Due to the particularity of this problem, most of the spectral-based methods have been developed for this issue. Wang *et al.* [1] were the first to advocate that the Aqua MODIS band 6 could be recovered by the stable analytical relationship between Terra MODIS bands 6 and 7. Their research was based on the observation that MODIS bands 6 and 7 are highly correlated in snow-covered areas. For recovering the Aqua MODIS band 6, the calibrated and geo-located Terra MODIS Level 1B radiances were employed. Polynomial regression was used to quantify the relationship between Terra MODIS bands 6 and 7. Reflectances at the top of the atmosphere (TOA) in Terra MODIS bands 6 and 7 were correlated with a correlation coefficient of 0.9821. Linear, quadratic, cubic, and fourth-degree polynomials were fitted to the data of Terra bands 6 and 7. Wang *et al.* [1] suggested using the following polynomials:

$$\mathbf{I}^6(x) = 1.6032\left(\mathbf{I}^7(\mathbf{x})\right)^3 - 1.9458\left(\mathbf{I}^7(\mathbf{x})\right)^2 + 1.7948\mathbf{I}^7(\mathbf{x}) + 0.012396 \quad (17)$$

or

$$\mathbf{I}^6(\mathbf{x}) = -0.70472\left(\mathbf{I}^7(\mathbf{x})\right)^2 + 1.5369\mathbf{I}^7(\mathbf{x}) + 0.025409 \quad (18)$$

where $\mathbf{I}^6(\mathbf{x})$ and $\mathbf{I}^7(\mathbf{x})$ are the reflectances of $p_{\mathbf{x}}$ at the TOA in Terra MODIS bands 6 and 7, respectively. Similar results can be obtained using these two polynomials. Wang *et al.* [1] emphasized that the relationship between these two bands depends on many factors, such as the scene type, the spectral

characteristics, and the scan geometry. The scene type in particular plays an important role. As (17) and (18) were developed based on snow cover, their performances are best for snow-covered scenes, and they show relatively large errors for scenes without snow cover [1]. For brevity, this method is called LF hereafter.

Rakwatin *et al*. [35] proposed to recover the missing data of Aqua MODIS band 6 by combining a histogram matching algorithm with local least squares fitting (HMLLSF). Histogram matching corrects the detector-to-detector striping of the functional detectors. Local least squares fitting recovers the missing data of the non-functional detectors, based on a cubic polynomial derived from the relationship between Aqua MODIS bands 6 and 7. The algorithm was tested on both Terra and Aqua MODIS images, and it can be used at both 1000-m and 500-m resolutions. Using simulated striped images of Terra MODIS data, the results of recovering the synthetic non-functional detectors of band 6 demonstrated that this method can recover the missing data with little distortion. Although this algorithm has greatly improved MODIS band 6 recovery, it does not consider the effect of different scene types.

Shen *et al*. [36] further found that the band relationship depends on the scene type. On this basis, they developed a within-class local fitting (WCLF) algorithm to recover the missing band 6 reflectances. An unsupervised classification is first performed to separate the various scene types, based on a band selection method. With the classification map, WCLF is performed to recover every single missing pixel in each type. Moreover, a refinement procedure is included in the local fitting process to eliminate the effect of outliers. Since the scene classification information is considered, the method can obtain a satisfactory result with complex surfaces. However, the result is heavily reliant on the classification map, especially for the pixels at the junction of different scene types.

The methods described previously reconstruct the missing information of band 6 only according to the spectral relationship of band 6 and band 7. However, for a product which has seven bands in total, the spectral relationship between the different bands is not fully utilized to reconstruct the missing information. Therefore, Gladkova *et al*. [37] proposed to build the relationships of band 6 and the other six bands for reconstruction (for 500-m resolution L1B data). On this basis, to take into consideration the local features, Li *et al*. [38] came up with the idea that band 6 and the other bands satisfy a stable relation function in a cluster of local patches. It is noteworthy that in different clusters of patches, the functions are different. The relationships can be roughly expressed as:

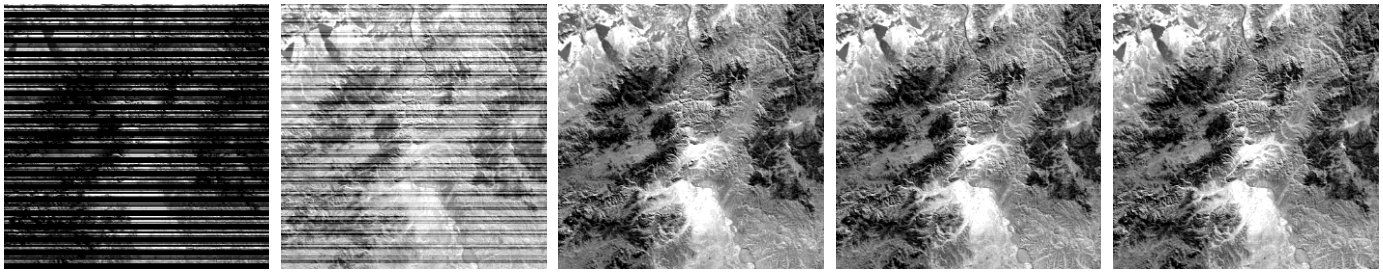

(a) (b) (c) (d) (e)

Fig. 11. Recovery results of Aqua MODIS band 6 using different methods. (a) The Original. Recovered images using the following: (b) the LF method in [1]; (c) the HMLLSF method in [35]; (d) the WCLF method in [36]; and (e) the RMEMR method in [38].

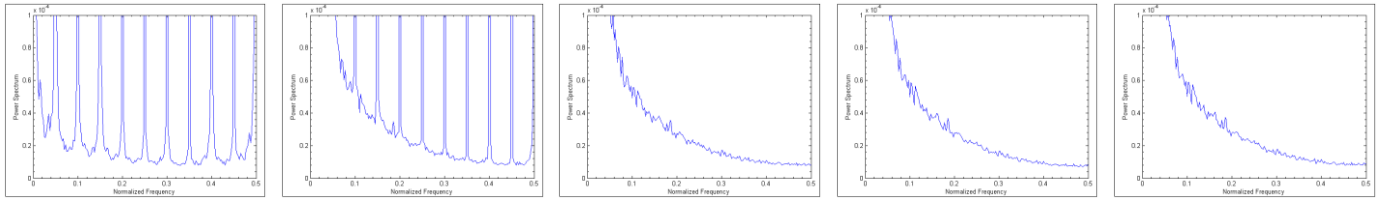

(a) (b) (c) (d) (e)

Fig. 12. (a)–(e) Spectrograms of Fig. 11(a)–(e).

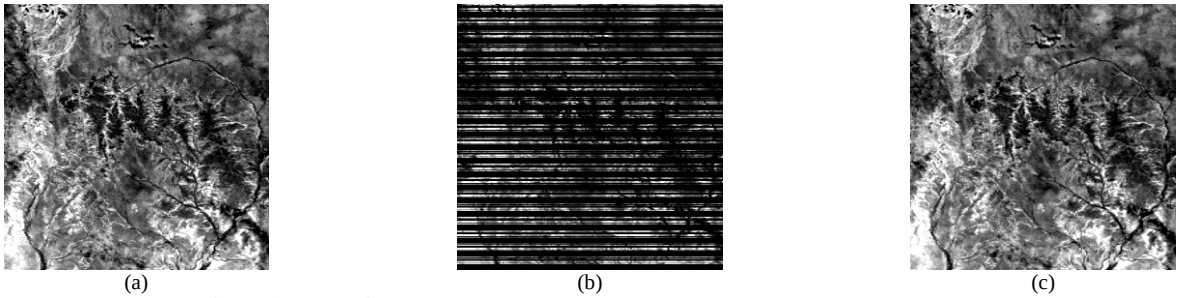

(a) (b) (c)

Fig. 13. Simulated reconstruction of the reflectance of Terra MODIS band 6. (a) The original image. (b) The corrupted image. (c) The recovery result of RMEMR.

TABLE II
QUANTITATIVE EVALUATIONS OF THE SPECTRAL-BASED METHODS

Methods	MAE	PSNR/dB
Corrupted	0.18420	13.0618
LF [1]	0.01805	32.0371
HMLLSF [35]	0.00494	42.7871
WCLF [36]	0.00421	43.4987
RMEMR [38]	**0.00212**	**49.1092**

$$\mathbf{I}^6(\mathbf{x}) = f_1\left(\mathbf{I}^1(\mathbf{x}), \mathbf{I}^2(\mathbf{x}), \mathbf{I}^3(\mathbf{x}), \mathbf{I}^4(\mathbf{x}), \mathbf{I}^5(\mathbf{x}), \mathbf{I}^7(\mathbf{x})\right), \mathbf{x} \in \mathbf{\Omega}^p \tag{19}$$

where $\mathbf{\Omega}^p$ denotes the local region of $\mathbf{I}$, and f_1 represents the relation function of band 6 and the other bands. The authors first utilized the good detectors in band 6 and the other bands to acquire the function f_1. f_1 was then used to reconstruct the missing information of the malfunctioned detectors in band 6. Since more spectral bands are made use of when the spectral relationships are being modeled, the methods of Gladkova *et al*. [37] and Li *et al*. [38] obtain better recovery results than the previous methods. The method proposed by Li *et al*. is called robust M-estimator multiregression (RMEMR).

We undertook a real data experiment on an Aqua MODIS image acquired on January 16, 2009, over North Korea. The original and recovery result images of the proposed algorithm are shown in Fig. 11. The test images in the experiment were of 400 by 400 pixels and a 500-m resolution. Fig. 11(a) shows the original band 6 image, with black stripes covering most of the image. Fig. 11(b)–(e) are the output images recovered by LF [1], HMLLSF [2], WCLF [3], and RMEMR [4], respectively. In Fig. 11(b), there are obvious stripes and artifacts. These results show that when the image contains complex terrain, it is difficult to fit the relationship between the two bands using only one band relationship curve. In Fig. 11(c)–(e), most of the recovered pixels match well. The three results are relatively close, but Fig. 11(c) is a little too smooth in the details.

Fig. 12 shows the Fourier transforms of the original and recovered data of the different algorithms. The horizontal axis represents the normalized frequency, and the vertical axis represents the average power spectrum of all the columns. In Fig. 12(b), the stripes are still clearly reflected in the frequency domain. Fig. 12(c)–(e) reveal similar smooth results.

Since the real data experiment did not show a difference between LF, HMLLSF, WCLF, and RMEMR, simulated experiments were also conducted to objectively evaluate the results of the spectral-based methods, in which the reflectance product of the same designed Terra MODIS (with Aqua MODIS) is artificially lost according to the same locations of Aqua MODIS. The experimental data are shown in Fig. 13. The visual effects of the results reconstructed by the four methods are very similar; thus, we just show the result of RMEMR in Fig. 13. The mean absolute error (MAE) and PSNR between the original and reconstructed results using the four methods, respectively, are shown in TABLE II. As can be seen, the four methods significantly improve the MAE and PSNR. In terms of the indicators, the order from the worst to the best is: LF, HMLLSF, WCLF, and RMEMR. Although the indicators of HMLLSF, WCLF, and RMEMR are different, for the reflectance product, they are so small that they can be considered as the same.

V. TEMPORAL-BASED METHODS

When the weather is cloudy, all the spectral bands of passive remote sensing data will be contaminated to different degrees. On the other hand, sensor malfunction can result in information loss in the same region of all the spectral bands. Accordingly, the spectral-based methods are no longer appropriate. As a result of the mobility of clouds and the scanning deviation of sensors, data over the same geographical region and acquired at different periods can provide supplementary information. For the temporal-based methods, the time interval is a double-edged sword. If the time interval is too short, the clouds in the two consecutive data sets will be mostly overlapping, and the temporal correlation may be ineffective. However, if the time interval is too long, the land cover can vary so greatly that the correlation is destroyed. Temporal differences are usually divided into three classes [2]: 1) differences caused by observation conditions; 2) differences caused by regular changes of geographical features (e.g., phenological changes); and 3) differences caused by the abrupt transformation of geographical objects (e.g., new buildings and man-made landscapes). Generally speaking, the temporal-based methods are appropriate for the first two kinds of temporal differences. It is noteworthy that the temporal-based methods have been investigated by the most scholars. The major temporal-based approaches include the temporal replacement methods [2-4], [39-47], the temporal filter methods [48-57], and the temporal learning model based methods [58], [59]. At the end of this part, we point out several special factors that should be considered when reconstructing the missing information of quantitative remote sensing data.

A. Temporal Replacement

Among the temporal-based methods, the classical approach is the temporal replacement methods. Fig. 14 shows the basic idea of the temporal replacement methods. In general, the temporal replacement methods can be classified into two counterparts: direct replacement and indirect replacement. When the time interval is so short that the temporal difference can be ignored, the direct replacement method does work. In other words, the missing information is replaced by information from the same region (region **S** in Fig. 14) in another referenced image. In this case, some scholars refer to this approach as mosaicing [60], [61]. When it comes to a temporal sequence of data, Lin et al. [3] and Holben [46] proposed to choose the optimal values among them. The direct replacement method obtains a good effect on the condition that the referenced data are very similar to the corrupted data. However, in real situations, due to the difference in atmospheric effects, sun angles, and sensor look angles during acquisition, there are always some differences in the brightness of pixels at the same location from different scenes. Thus, the direct replacement method cannot work on most occasions.

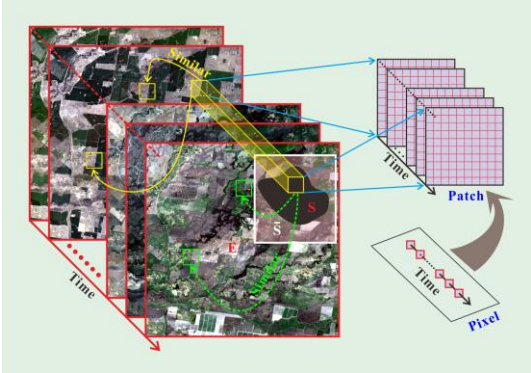

Fig. 14. Temporal replacement.

When the direct replacement cannot work, a number of researchers have resorted to indirect replacement. The reason why the direct replacement does not work is that temporal differences exist. It is therefore necessary to reduce the differences. To minimize the differences/variations, a correction/transformation is needed. The fundamental formula is as follows:

$$\hat{\mathbf{I}}_{T_0}(\mathbf{x}_0) = f_2\left(\mathbf{I}_{T_1}(\mathbf{x}_0), \mathbf{I}_{T_2}(\mathbf{x}_0), \cdots, \mathbf{I}_{T_i}(\mathbf{x}_0), \cdots\right) \quad (20)$$

where $\hat{\mathbf{I}}_{T_0}(\mathbf{x}_0)$ is the estimated value of an attribute at the point of interest $\mathbf{x}_0$ acquired at time T_0, $\mathbf{I}_{T_i}(\mathbf{x}_0)$ is the value observed at time T_i, and $f_2(\cdot)$ is the correction function. After this correction, the time-series data are more similar to each other, so the replacement can be continued. It is noteworthy that the correction is usually undertaken according to the whole of the remaining data (region $\mathbf{E}$ in Fig. 14) [3], [42]. For a better consideration of the local correlations, neighborhood (region $\bar{\mathbf{S}}$ in Fig. 14) correction of the missing region has been proposed [4], [43]. In fact, as far as the principle is concerned, the temporal fitting methods [39], [40] also belong to this category. Generally speaking, the temporal replacement can be carried out pixel-by-pixel [46], patch-by-patch [3], [44], or by the whole of the missing region [42], [60], [61]. However, because of the errors of registration and the abrupt changes in land cover, the temporal replacement may result in an aliasing phenomenon.

The temporal replacement methods are usually used in cloud removal and random gap filling. In [60], cloudy IKONOS images were recovered by temporal replacement and gray-level balancing. Tseng et al. [63] replaced the cloud and cloud shadow zones of a SPOT image by the cloud-free zones on other images, and adjusted the pixel values using color statistics. To solve the ETM+ SLC-off problem, the USGS Earth Resources Observation and Science Center (EROS) suggested that the un-scanned gaps could be compensated for by previous SLC-on images of the same area [62]. A simple histogram matching method was adopted. As the gap-covered locations vary in the different scenes, this allows the possibility of restoring the missing pixels with multitemporal SLC-off data. An improved method using multiple SLC-off images was subsequently developed by the EROS data center (EDC), where every missing value is obtained by employing a local linear histogram matching (LLHM) in a moving window. This method is very simple and easy to implement, and can perform well in most regions if the input scenes are of high quality. Nevertheless, it tends to be more sensitive with regard to data selection, and has difficulty with heterogeneous landscapes where the features are smaller than the local moving window size [64]. Chen et al. [65] developed a method known as the neighborhood similar pixel interpolator (NSPI), where the missing information is reconstructed by combining replacement and interpolation, and it was found that NSPI can restore the value of un-scanned pixels accurately, even in

(a) (b) (c) (d) (e) (f)

Fig. 15. Landsat SLC-on ETM+ images for the simulated experiment: (a)–(b) images acquired on March 19, 2002, and December 29, 2001, respectively; (c) SLC-off image simulated from (a). (d), (e), and (f) are the results recovered by direct replacement of (b), LLHM [62], and WLR [2], respectively.

(a) (b) (c) (d) (e)

Fig. 16. Landsat ETM+ cloudy images: (a)–(b) are the original images. (c), (d), and (e) are the results recovered by direct replacement of (b), LLHM [62], and WLR [2], respectively.

heterogeneous regions. Zeng et al. [2] proposed a multitemporal weighted linear regression (WLR) method to adjust the replacement information adaptively, and the method can predict the missing values very accurately in varied scenes.

Our first experimental region is located in Wuhan, China, around 30.59 ℃N and 114.02 ℃E, and is covered by Path 123 and Row 39 in World Reference System 2 (WRS-2). Fig. 15(a) and (b) show the two test ETM+ images (true color composite R=band 3, G=band 2, B=band 1) acquired on March 19, 2002, and December 29, 2001, respectively. The input primary image covered by simulated gaps is shown in Fig. 15(c). Fig. 15(d)–(f) are the output images recovered by direct replacement, LLHM, and WLR, respectively. In general, the image recovered by the WLR method appears much closer to the actual image [Fig. 15(a)] than the results of the other two methods. In Fig. 15(d), the replaced pixels are clearly different from those in the original image. In Fig. 15(e), for LLHM, obvious artifacts can be found near the edge of the river. This result shows that when the image contains complex terrain, a simple linear algorithm using all the common pixels is unsatisfactory. In Fig. 15(f), for WLR, all the edges are well recovered, even at the border of small objects.

To better illustrate the effect of the different methods, an experiment using a cloud-contaminated image was also implemented. Fig. 16(c)–(e) are the output images recovered by direct replacement, LLHM, and WLR, respectively. The results are similar to the results of the simulated experiment. The replacement method obtains a very poor result, the LLHM-recovered pixels are not satisfactory in the edge regions, while the WLR method gives the best visual effect.

B. Temporal Filter

The temporal filter methods are commonly used in eliminating the noise in one-dimensional signals, which can be seen as a single point of a time series in remote sensing data, according to certain criteria. These methods are based on the fact that time-series data are strictly chronological and display regular fluctuations. The temporal filter methods can be grouped into three types according to the way they handle the data. Fig. 17 shows a brief schematic.

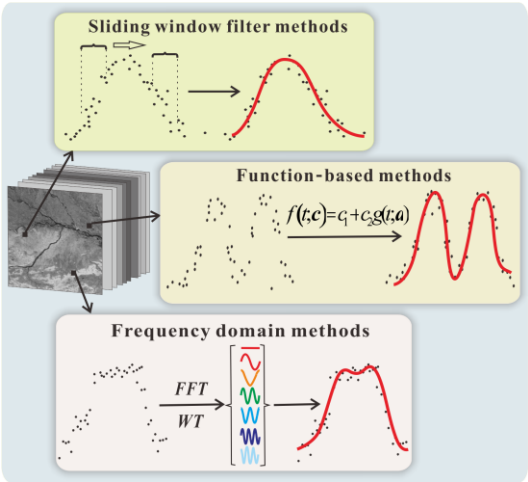

Fig. 17. The temporal filter methods.

1) Sliding Window Filter Methods: These methods are designed to filter in sliding windows, according to certain criteria, and are primarily used for reconstructing NDVI time-series data [48], [51-54]. The two most common and classical methods are the best index slope extraction (BISE) method [52] and the adaptive Savitzky-Golay (SG) filter [66], which have been successfully used in many studies. The BISE method and the SG filter are both based on the predictability of the vegetation change.

The BISE method is designed as a forward searching strategy within a sliding period. The next point should be compared with the first point, and the next point is acceptable when the value is larger. The threshold for an acceptable percentage increase should be determined empirically when the next point value is smaller [48]. The disadvantage of this method is that it is subjective to determine a reasonable length of sliding period and the threshold [55].

The SG filter is a simplified local least squares fitting convolution for smoothing and computing derivatives of a set of consecutive values [48]. The SG filter can be described as follows:

$$\hat{\mathbf{I}}_t(\mathbf{x}) = \frac{\sum_{i=-l}^{l}\left(b_i \mathbf{I}_{t+i}(\mathbf{x})\right)}{2l+1} \tag{21}$$

where $\mathbf{I}_{t+i}(\mathbf{x})$ is the original value of point $p_{\mathbf{x}}$ acquired at time $t+i$, $\hat{\mathbf{I}}_t(\mathbf{x})$ is the reconstructed value, b_i is the weight of $\mathbf{I}_{t+i}(\mathbf{x})$, and $(2l+1)$ is the length of the convolution window, which not only determines the smoothness of the results, but also greatly influences the ability to rapidly fit changing time-series data.

2) Function-Based Curve Fitting Methods: These methods include the asymmetric Gaussian (AG) model [56] and the double logistic (DL) technique [57], and they are commonly used for the outer envelope of NDVI time-series data, based on least squares fitting. They are the most commonly used ways of fitting time-series data [67], [68] and have been integrated into the TIMESAT software by Jönsson and Eklundh [49] for analyzing time-series satellite data.

A general fitting model, as shown in (22), can describe both the symmetric Gaussian function fitting method and the DL function fitting method.

$$f_3(t;\mathbf{c}) = c_1 + c_2 g(t;\mathbf{a}) \tag{22}$$

where $\mathbf{c}=[c_1,c_2]$ are the linear parameters, $g(t;\mathbf{a})$ is the basis function and $\mathbf{a}$ is its parameter, and t has the same meaning as in Section II.

For the symmetric Gaussian function, the basis function can be described as follows:

$$g(t;\mathbf{a}) = \begin{cases} \exp\left[-\left((t-a_1)/a_2\right)^{a_3}\right], & if\ t > a_1 \\ \exp\left[-\left((a_1-t)/a_4\right)^{a_5}\right], & if\ t < a_1 \end{cases} \tag{23}$$

where a_1 determines the position of the maximum or minimum

with respect to the independent time variable t, and a_2 (a_4) and a_3 (a_5) are the width and flatness of the right (left) function, respectively [49], [56].

For the DL function, the basis function is selected as follows:

$$g(t;\mathbf{a}) = \frac{1}{1+\exp\left((a_6 - t)/a_7\right)} - \frac{1}{1+\exp\left((a_8 - t)/a_9\right)} \quad (24)$$

where a_6 is the point where the curve increases, a_7 is the rate of increase at this point, and a_9 is the rate of the decrease at the decreasing inflection point a_8. Beck *et al*. [57] expanded the details of this algorithm to fit an NDVI time series. The parameter **a** for both of these two functions should lie within specified ranges to ensure the smooth results of the model simulation. Song *et al*. [67] made a comparison for the two function-based methods and the SG filter by applying them to the MODIS 16-day composite 250-m NDVI products.

3) Frequency Domain Methods: The Fourier transform is a very effective analysis method in treating periodical time-series signals, which decomposes the signals into amplitude and phase information, based on the cosine decomposition of the harmonics. A fast Fourier transformation (FFT) is often used for saving calculation time. Seller et al. [69] first applied the method to an AVHRR NDVI time series by fitting the first three harmonics with a least squares solver [56]. Similarly, the harmonic analysis of time series (HANTS) method was proposed in [70], and has been successfully used in reconstructing cloud-free NDVI composites [50]. In this algorithm, only the most significant frequencies are used in the time profiles, and a least squares curve fitting procedure is applied, based on the harmonic components.

The wavelet transform (WT) can analyze signals in time-frequency space and it can efficiently identify and reduce noise while maintaining useful information in time-series data [55]. Lu et al. [55] proposed the wavelet-based method to remove contaminated data from time-series observations. In this method, a quality flag and the blue band are first used to linearly interpolate the time-series data, and then to reconstruct the new time-series data using the highest correlation adjacent scales after decomposing the time series into different scales, which is more credible and robust than the threshold-based method.

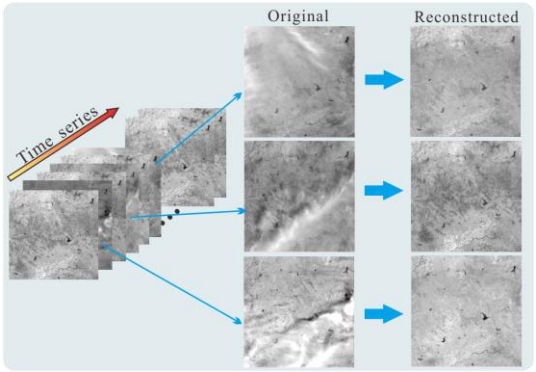

Fig. 18. Comparison of the cloud-contaminated MODIS reflectance products before and after temporal reconstruction.

On the whole, although the methods mentioned above are mainly used to restore the NDVI, they can also be applied to other parameters that have similar characteristics to those of time-series NDVI, with some adjustments. A characteristic of these methods that should be pointed out is that the pixel values of the reconstructed results all show little difference from the original values. Fig. 18 shows the results of the cloud-contaminated MODIS reflectance products before and after temporal reconstruction.

C. Temporal Learning Model

Most of the temporal-based methods for reconstructing missing information attempt to build a clear function relationship (linear or nonlinear) between the corrupted data and other good data in the temporal domain. In recent years, attempts have been made to establish an unknown relationship by the approach of temporal learning, under the perspective of compressed sensing (CS) or sparse representation. The representative methods were proposed by Lorenzi et al. [58] and Li et al. [59]. Lorenzi et al. proposed to obtain the CS solution through a formulation within a genetic optimization scheme, and Li et al. considered it as a multitemporal dictionary learning issue. Additionally, in [71], Latif et al. proposed a nonparametric regression Kohonen's self-organizing map (SOM) algorithm by learning mode to reconstruct the missing values in the low-resolution time series MODIS, in which the result is very promising. At present, the temporal learning methods are just in the infant stage, but have already shown certain advantages. These methods are introduced in Section VI-B.

D. Special Factors for Quantitative Data

Quantitative data are a special kind of remote sensing data that are retrieved from remote sensing spectral data. Quantitative data include the NDVI, LST, leaf area index (LAI), albedo, aerosol, and ozone, and they have been widely used in many study areas [68], [69], [72]. Similarly, they suffer from the missing data problem, as remote sensing spectral data do. Although several simple compositing techniques, such as the maximum-value composite (MVC) method [46] and the average (AVG) approach [73], have been proposed, they not only reduce the temporal resolution of the quantitative data, but they also cannot eliminate the total atmospheric influences.

In fact, each of these quantitative products shows different attenuations according to their own characteristics, so some special factors should be considered in the reconstruction process. For example, the NDVI values range from to 1, where a minus value indicates a low vegetation coverage. Therefore, for some methods, the pixel value range is an important factor to be considered. When reconstructing NDVI time-series data, two other factors should be considered, in that the data are basically related to vegetation change, and the NDVI values are depressed when affected by clouds and poor atmospheric conditions. Thus, keeping the high values in the reconstruction process is feasible. The NDVI composite products are mainly calculated through the MVC technique, and several approaches

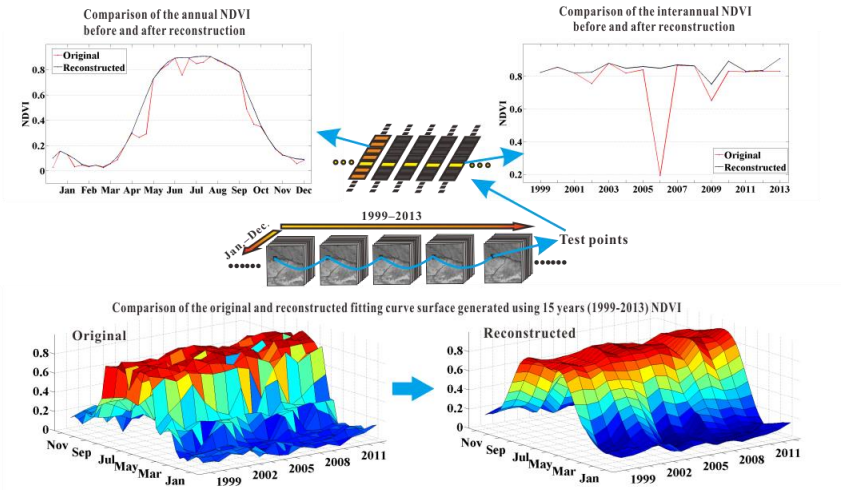

Fig. 19. Comparison of SPOT VEGETATION 10-day MVC NDVI products before and after reconstruction from different perspectives.

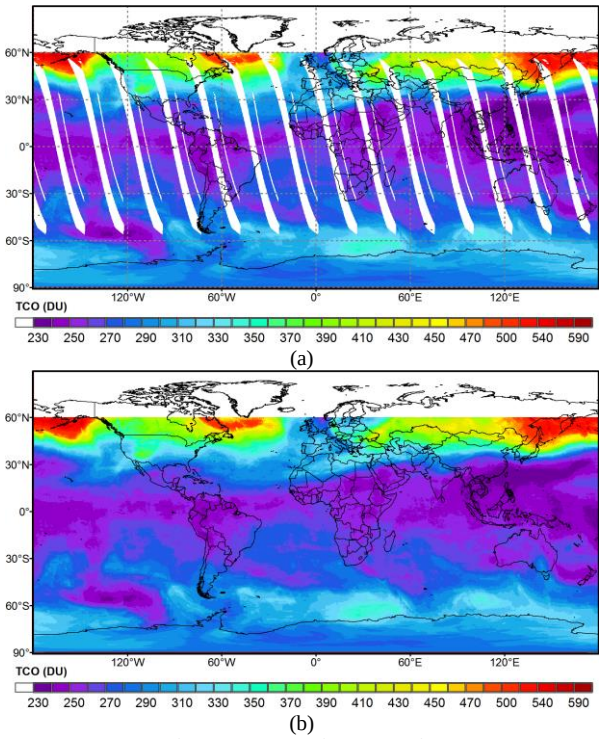

Fig. 20. Ozone data of Aura OMI before and after reconstruction. TCO represents total column ozone and DU means Dobson unit. (a) Before reconstruction. (b). After reconstruction.

have been proposed to make the data approach the upper NDVI envelope [48], [51], [53]. Fig. 19 shows an example of NDVI data before and after reconstruction from different perspectives. In addition, the ecological classification and spatio-temporal variation are important factors that should be taken into consideration. For example, within a small region, pixels of the same ecosystem classification should exhibit roughly the same phenological or temporal behavior. However, pixels show different ecological behaviors under different growth conditions. Based on this consideration, a number of methods have been developed to fill the missing data for albedo and LAI products [72], [74].

As for atmospheric products (e.g., aerosol optical depth and ozone), the characteristic of highly random variation makes the reconstruction more complicated. Fig. 20 shows the ozone data acquired by Aura OMI before and after missing information reconstruction. The impact of atmospheric flow cannot be ignored in multitemporal reconstruction. Furthermore, physical facts should also be considered [41], [75]. For example, for LST reconstruction, the LST under clouds is lower than the cloudless LST, as the solar radiation is partly hidden by the clouds. As a consequence, the hidden solar radiation must be taken into account to obtain the real LST.

VI. Hybrid Methods

The three kinds of methods stated previously all have their strengths and weaknesses, and they all depend on the correlations in only one kind of domain (spatial domain, spectral domain, or temporal domain). As a result, they are powerful in some cases, but also powerless in certain other cases. Correspondingly, it is possible to combine their individual strengths to reconstruct the missing information. The hybrid methods attempt to make better use of the correlations hidden in the spatial, spectral, and temporal domains. Existing examples of the hybrid methods include the joint spatio-temporal methods [2], [45] and the joint spatio-spectral methods [43].

A. Joint Spatio-Temporal Methods

1) Successive Utilization of Spatial and Temporal Methods: Hybrid methods usually combine two or more of the above methods. The most basic idea is to successively implement a method based on the result of another method. In the method proposed in [2], a temporal-based method is first used, and then a spatial-based regularization method is used when the multitemporal data cannot completely recover all the missing pixels. In this two-step method, both the temporal information and the spatial information are used, respectively. As an example, the experimental ETM+ images acquired on October 23, 2011, and November 8, 2011, around 39.10 ℃N and 76.14 ℃W, are shown on the left of Fig. 21. After temporal replacement, although some areas are well reconstructed, as the gaps cannot

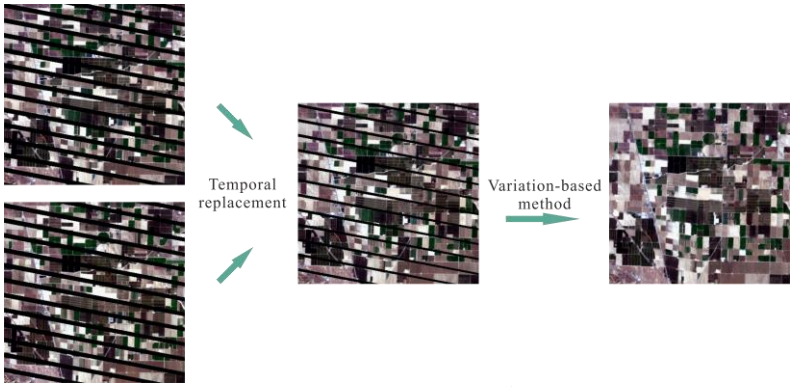

Fig. 21. Reconstruction results using successive utilization of spatial and temporal methods [2].

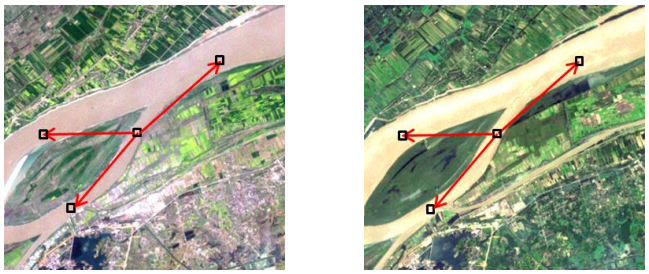

(a) (b)

Fig. 22. Two different scenes (a) and (b).

be completely covered by the auxiliary image (the lower one on the left of Fig. 21), there are still invalid pixels remaining in the recovered image. A Laplacian prior regularization method is then performed to recover the remaining invalid pixels. This two-step strategy is effective and easy to operate. However, as the reconstruction is not implemented under a unified framework, there may be obvious differences between the areas reconstructed by the different methods.

2) Spatial Completion With Temporal Guidance: As stated previously, since the successive utilization of spatial and temporal information does not make the best use of the correlations in the two domains, some scholars have proposed a unified framework: spatial completion with temporal guidance [13], [45]. For example, Cheng et al. [45] proposed a novel cloud removal method that merges the ideas of the spatial-based category and the temporal-based category. This method recovers a missing pixel by utilizing the similar pixels within the corrupted image itself, while another scene image is used as guidance. The approach is based on the fact that the relative positions of similar pixels within an image are generally coincident with another scene acquired at a different time, although multitemporal images will usually show some changes because of the different atmospheric conditions or seasonal situations. The similar pixels are assumed to have similar change trends in the multitemporal images. As shown in Fig. 22, the locations marked with black squares, which are similar pixels in image (a), are also similar pixels in image (b). That is to say, another scene can guide us to find the positions of the similar pixels. Therefore, the solution for cloud removal in [45] is as follows: a missing pixel is filled using an appropriate similar pixel within the remaining regions of the corrupted image, and another reference image is used as guidance to locate the similar pixels. In order to ensure the global coherence of the reconstruction image, a pixel-offset based spatio-temporal MRF (STMRF) global function is built to jointly select the most suitable similar pixels in the remaining regions to replace the missing pixels. This STMRF method combines the advantages of the spatial-based methods, which reconstruct the data using the radiometric information in the corrupted image itself to ensure that the recovery keeps a high degree of spectral coherence and a convincing visual quality, and the temporal-based methods, which guarantee the fine information accuracy of the reconstruction results.

Fig. 23 illustrates the superior performance of this spatial completion method with temporal guidance. Fig. 23(a) is the original MODIS image acquired on August 2, 2010, and Fig. 23(b) is the reference image acquired on March 11, 2010. Fig.

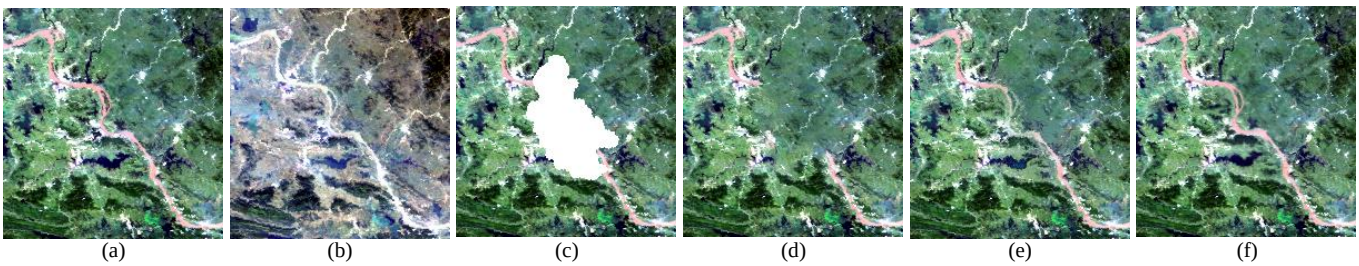

(a) (b) (c) (d) (e) (f)

Fig. 23. Experimental results for the recovery of a cloudy image. (a) Original MODIS image acquired on August 2, 2010. (b) Reference image acquired on March 11, 2010. (c) Cloud-contaminated image simulated from (a). Recovered images using the following: (d) the spatial-based method in [19]; (e) the temporal-based method in [22]; and (f) the spatial completion method with temporal guidance in [45].

23(c) is the cloud-contaminated image simulated from Fig. 23(a). To allow a comparative analysis, this hybrid method was compared with a spatial-based method and a temporal-based method, and their reconstruction results are shown in Fig. 23(d)–(f). From Fig. 23(d)–(f), it can be seen that the result of this joint spatio-temporal method is clearly better than the individual spatial-based and temporal-based methods. When the terrain is complex and the missing region is large, the recovery result of the spatial-based method [Fig. 23(d)] is inaccurate, and the correlation coefficient (CC) calculated from the cloud-contaminated region for this result is just 0.70263. In the result of the temporal-based method [Fig. 23(e)], most of the ground features are recovered well, but in the river region, the spectral characteristic is still different from that in the remaining river region, which may also be a result of the large spectral differences between the corrupted image and the reference image. The CC for this result is 0.83804. For the joint spatio-temporal method, it shows the most plausible visual result, some of the detailed information is recovered well, and the reconstructed region is the most consistent with the original image. The CC for this result is the highest, with a value of 0.86527. It is worth noting that the two input images were acquired in different seasons, and the spectral characteristics of the ground features are significantly different. Most of the temporal-based methods cannot effectively deal with such a difference. However, the joint spatio-temporal method is better able to address the issue.

B. Joint Spatio-Temporal Methods

As is well known, the spectral correlations and temporal correlations are the basic properties of remote sensing data. When the two correlations are available, it is clearly not enough that only one of them is utilized. Therefore, the joint spectral-temporal idea is a promising approach. Currently, the joint spectral-temporal methods [76] are few in number. Here, we introduce one primary example in the framework of sparse representation. Sparse representation has been applied to the reconstruction of the missing information of remote sensing data, e.g., the aforementioned spectral-based methods [18], [77], [78] and temporal-based methods [58], [59], [79]. Their main differences lie in the data organization.

Firstly, it is necessary to review sparse representation. Sparse representation has drawn the attention of a large number of researchers in recent years. The superiority of the approach is that it has been shown to be able to approximately reconstruct the original signal, with a high probability, by the use of just a small amount of observed information. Sparse representation requires that the data itself are sparse or are sparse in a certain domain. Usually, remote sensing data do not directly meet the requirement. However, the data often include a large amount of redundant information, which means that the data can be transformed into a sparse domain by dictionary learning, meaning that the data are sparse in a learned basis set. The basis, also called the overcomplete dictionary, is composed of a series of incoherent atoms. Thus, the data can be represented by a linear combination of a few learned atoms. For brevity, in the framework of sparse representation, the joint spectral-temporal method is described below. Note that the joint spectral-temporal method can also be applied to just multispectral data or just multitemporal data.

Suppose that T observed multitemporal remote sensing data are denoted by $\{\mathbf{J}_t\}_{t=1}^{T}$, and $\mathbf{J}_t \in \mathbb{R}^{m\times n\times k}$ is a term of the multispectral data which may include the missing information. For the convenience of description, we consider that $\mathbf{J}_1^1$ does include the missing information. In this situation, it is insufficient to extract the complementary information only from the spectral domain or only from the temporal domain. In order to extract more useful information, the spectral and temporal components should be simultaneously used. In other words, $\{\mathbf{J}_1^i\}_{i=1}^{k}$ and $\{\mathbf{J}_t^1\}_{t=2}^{T}$ consist of 3D data $\mathbf{Y}_0 \in \mathbb{R}^{m\times n\times H}$ $(H=k+T-1)$. The spectral and temporal differences reside in $\mathbf{Y}_0$. To reduce them, excluding $\mathbf{J}_1^1$ (the component to be reconstructed), the components of $\mathbf{Y}_0$ are normalized to the referenced component $\mathbf{J}_1^1$ using a linear or nonlinear transformation, according to their shared existing information. After normalization, the components of $\mathbf{Y}_0$ will be reordered, based on their correlations with $\mathbf{J}_1^1$. The stronger the correlation to $\mathbf{J}_1^1$, the closer the order to $\mathbf{J}_1^1$. $\mathbf{Y}_0$ will then become a new 3D data cube $\mathbf{Y}$. With the help of a patch operation and a stack operation [80], the sparse representation of $\mathbf{Y}$ becomes available. Fig. 24 shows the result of data organization and the process of patch extraction. A typical energy minimization of the missing information reconstruction issue is usually expressed as follows:

$$\arg\min_{\mathbf{X},\boldsymbol{\alpha}_{ij}} \lambda\left\|\mathbf{M}\mathbf{X}-\mathbf{Y}\right\|_2^2+\sum_{ij}\mu_{ij}\left\|\boldsymbol{\alpha}_{ij}\right\|_0+\sum_{ij}\left\|\mathbf{D}\boldsymbol{\alpha}_{ij}-\mathbf{P}_{ij}\mathbf{X}\right\|_2^2 \quad (25)$$

where $\mathbf{M}$ is a mask signifying where the information is missing, as in (8), $\mathbf{X}$ is the ideal data (of $\mathbf{Y}$) to be reconstructed, $\mathbf{P}_{ij}$ is an operator which extracts the (ij) patch from the data cube, $\mathbf{D}$ is the overcomplete dictionary, $\boldsymbol{\alpha}_{ij}$ are the sparse coefficients of the (ij) patch, and λ and μ_{ij} are the corresponding regularization parameters. This expression purports to show an approximation between the observed data

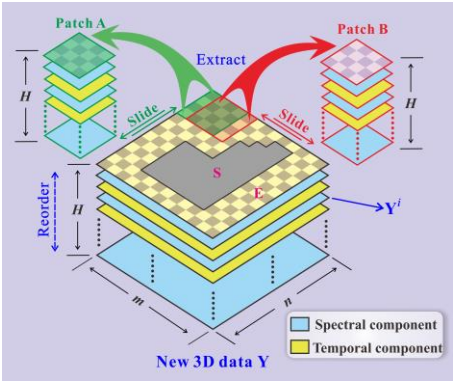

Fig. 24. Remote sensing data organization and patch extraction.

$\mathbf{Y}$ and the unknown ideal counterpart $\mathbf{X}$, only for the valid or existing data. The second and third terms of (25) are the local sparse priors of the data, which guarantee that every patch of the recovered data has a sparse representation.

In order to show the differences between the reconstruction results of the spectral-based, temporal-based, and joint spectral-temporal methods, in the framework of sparse representation, a group of simulated experiments were conducted with MODIS reflectance L1B 500-m resolution products. For the spectral-based method, the experiment utilized seven bands, and a partial region of one band was artificially removed [see Fig. 25(a)]. For the temporal-based method, the experiment utilized seven reflectance products from different times, and the missing information was the same as for the spectral-based method. It is noteworthy that the numbers of extra data components were the same in both the spectral-based and temporal-based experiments. For the joint spectral-temporal method, the experimental data were the total of the spectral-based and temporal-based methods. Fig. 25 shows the visual results of the reconstruction. As shown in Fig. 25, as far as the overall effect is concerned, the three methods effectively recover the missing information. However, in terms of the zoomed-in yellow-box regions, the effect can be ranked from the best to the worst: 1) the joint spectral-temporal method; 2) the spectral-based method; and 3) the temporal-based method. The land-surface features can change in the multitemporal data, which results in the worst reconstruction result when using the temporal-based method. The joint spectral-temporal method obtains the best result because it combines the advantages of the spectral and temporal domains. TABLE III shows the quantitative evaluations of the three methods, in which the MAE, mean relative error (MRE), and CC between the reconstructed result and the original are considered as the indicators. Again, the joint spectral-temporal method obtains the best result.

Fig. 26 shows the MRE variation diagram for the reconstruction results of Fig. 25, based on the three methods, with different numbers of complementary data terms (spectral and temporal). As the data number is varied, at first the spectral-based method obtains the lowest MRE, and then when the number is sufficient, the MRE of the joint spectral-temporal method becomes the lowest. This is because when the data are insufficient, the ability of the joint spectral-temporal method cannot be made best use of. Overall, however, the joint spectral-temporal method obtains the most stable result. This experiment demonstrates that the most significant advantage of the joint spectral-temporal method is the stability. Although it obtains a better quantitative result than the spectral-based method and the temporal-based method with sufficient data, it is not as good as the spectral-based method with only a small amount of data.

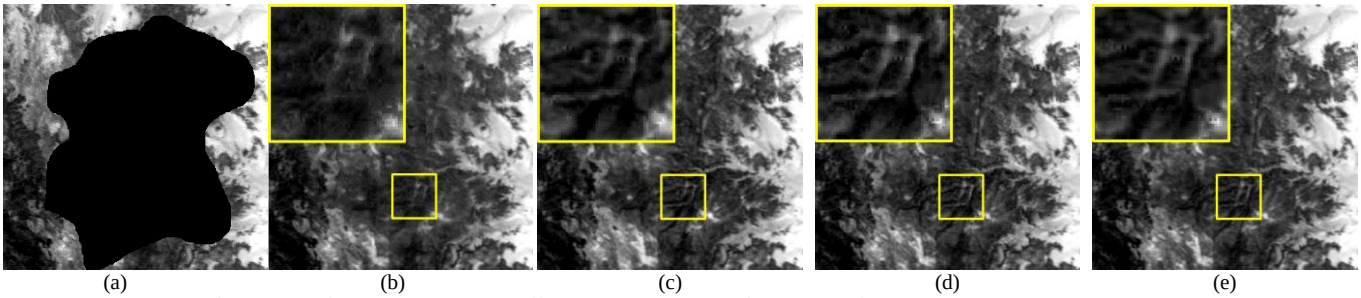

(a) (b) (c) (d) (e)

Fig. 25. Reconstructions of MODIS reflectance data using different methods, in the framework of sparse representation. (a) Corrupted data with missing information. (b) Result of the temporal-based method. (c) Result of the spectral-based method. (d) Result of the joint spectral-temporal method. (e) Original data.

TABLE III
COMPARISONS BETWEEN THE RECONSTRUCTIONS OF THE SPARSE REPRESENTATION METHODS IN FIG. 25

Methods	MAE/10^{-3}	MRE/%	CC
Corrupted	66.9471	52.2133	0.6579
Spectral	3.5181	2.7268	0.9898
Temporal	3.5851	2.8329	0.9898
Spectral-temporal	**2.9971**	**2.3490**	**0.9931**

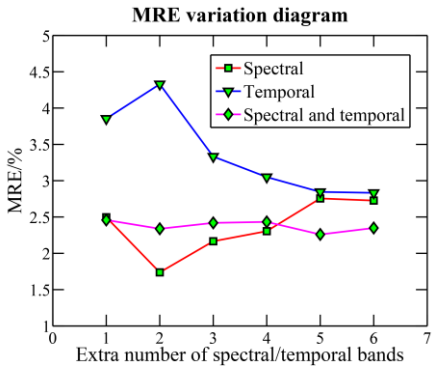

Fig. 26. The MRE variation diagrams of the reconstructions result for Fig. 25, based on the spectral-based method, the temporal-based method, and the joint spectral-temporal method, respectively, with different extra numbers of spectral/temporal bands.

VII. DETERMINATION OF MISSING LOCATION AND ERROR EVALUATION

As far as missing information reconstruction of remote sensing data is concerned, the precondition is that the missing location is known. Therefore, how to detect the missing location is important for the missing information reconstruction. On the other hand, the reconstruction accuracy is also worthy being paid attention to.

A. Determination of Missing Location

In terms of reconstruction of missing information, the first

step is to detect the missing information itself. For the sensor failure case, the detection is very simple or the missing location is recorded in the data header file. However, clouds in remotely sensed images are distinct, which can be detected based on its spectral, thermal and spatial features. The cloud amounts calculated by the cloud screening algorithms are often provided accompanied with the remote sensing images and products. Taking Landsat ETM+ data for example, the automatic cloud cover assessment (ACCA) method was designed to estimate the percentage of the cloud amount in a scene [81]. For MODIS data, as a cloud product, MOD35 not only estimates the cloud amount, but also provides cloud masks by using 48 bits to mark the locations and probabilities of cloudy pixels [82]. Several object, decision tree, neural network and multi-temporal based methods were also explored to improve the cloud detection accuracy [83-86]. Additionally, radiometric and geometric feature based clouds detection methods are also promising when the observation platform is equipped with panchromatic and multispectral observation ability (e.g., Quickbird and Pleiades) [87]. Current studies show that the cloud detection precision can be over 90% in most situations. In general, determination of missing location has a great impact on the reconstruction accuracy. Specially, omitting is a fatal failure for reconstruction because the corresponding locations cannot be reconstructed. Thus, in the process of determination of missing location, it is allowed that the good location is detected as missing location, but omitting the missing location cannot be allowed absolutely. Additionally, in order to achieve a better reconstruction, the usual way of doing is to appropriately dilate the determination result of missing location.

B. Error Evaluation

It is an important work to evaluate the accuracy of the reconstruction results. By now, there have been a number of error evaluation methods on the reconstruction results, and we will give a brief review as follows.

1) Qualitative Evaluation: For a single remote sensing data term, researchers often resort to the visual effect, including brightness, structural continuity, etc. This scheme is effective to some degree, however, accompanied with subjectivity. If the data is multi/hyperspectral, the spectral profile [88] is also considered as an available method to assess the spectral fidelity. The closer the shape of the reconstructed spectral profile to the referenced one, the better the result. For a series of remote sensing data, similar to the spectral profile of multi/hyperspectral data, the temporal profile [89] can be used for the temporal consistence and variation of multitemporal data. For a long time series of remote sensing data, this evaluation method is suitable.

2) Quantitative Evaluation: On one hand, the quantitative evaluation is used for simulated validation. An original image is first degraded by removing some pixels, and then is used as the reference for the reconstructed result. Usually, the evaluation indicators include SSIM, mean squared error (MSE) [59], MRE, MAE, CC, PSNR, spectral angle (SA, for multi/hyperspectral data) [90], universal image quality index (UIQI) [2], [91], and many others. Based on these indicators, we can get a relatively objective evaluation. On the other hand, cross-validation is available when the alternative data exist, for example, the ground site data and higher precision (than the reconstructed data) sensed data from other satellite platforms.

3) Task-Oriented Evaluation: Different tasks need different reconstruction accuracies. Therefore, the task-oriented error evaluation methods have been proposed in recent years. In other words, researchers can measure the reconstruction error from the perspective of the influence on the subsequent task, such as classification [4], [47], [58], [89], vegetation change monitoring [71] and so on. The authors in [43] firstly generated the error map to convey the reconstruction reliability to the end-users, which is a creative work.

VIII. Conclusion and Prospects

As a result of the inside and outside factors of the remote sensing platforms, it is a common phenomenon that the acquired data are subject to missing information. This problem seriously affects the practical applications of remote sensing data. Thus, precise reconstruction of the missing information is of great significance for the data analysis and interpretation. In the past decades, a large number of algorithms have been proposed to reconstruct the missing information of remote sensing data. According to the source of the complementary information, the methods have been classified into four categories in this review: 1) spatial-based; 2) spectral-based; 3) temporal-based; and 4) hybrid. In this review, we have surveyed the strengths and weaknesses of these methods, both theoretically and experimentally.

However, for this complicated and ill-posed inverse problem, the current research still has room for improvement. Based on the development status, to the best of our knowledge, we believe that the promising directions include: 1) how to better utilize the correlations in the spatial, spectral, and temporal domains (spatio-spectro-temporal integration); 2) the use of more data sources with complementary information (multisource fusion); and 3) the development of high-efficiency and high-accuracy algorithms; 4) the development of task-oriented algorithms; 5) the generalization of missing information reconstruction.

A. Spatio-Spectro-Temporal Integration

As stated previously, the spatial-based methods make use of the correlations in the spatial domain (local and nonlocal correlations), and are ineffective in reconstructing large-area missing information. The spectral-based methods are competent approaches for reconstructing large-area missing information, based on the spectral correlations, but they cannot be used with thick cloud cover. The temporal-based methods are almost custom-made techniques for cloud cover, but they are sensitive to land-cover changes, especially abrupt changes. Therefore, it makes sense to simultaneously take advantage of the strengths of all three methods. To date, there have been some methods proposed that integrate two of the three methods, e.g., the joint spatio-spectral methods [43] and the joint spatio-temporal methods [92]. Generally speaking, we think

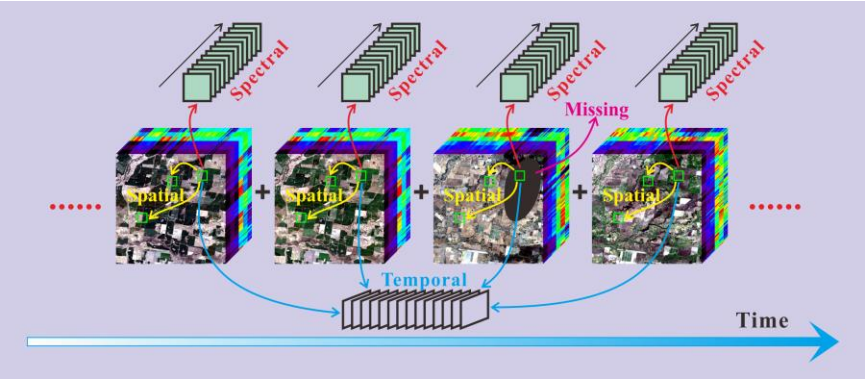

Fig. 27. Spatio-spectro-temporal integration.

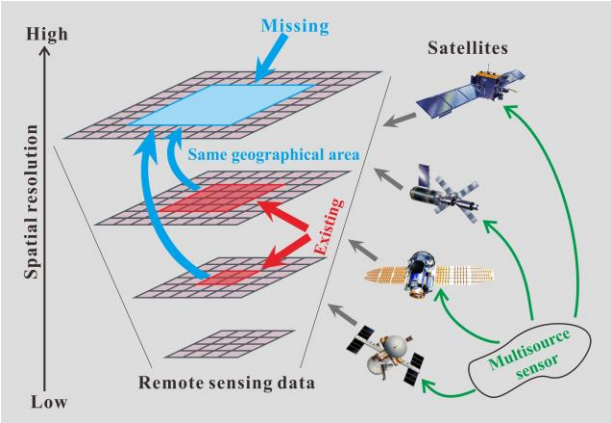

Fig. 28. Multisource data fusion.

that spatio-spectro-temporal integration, as shown in Fig. 27, will become the trend in missing information reconstruction. However, the key point is to determine the degree of contribution of the spatial, spectral, and temporal domains.

B. Multisource Fusion

For all the spatial-based methods, the spectral-based methods, the temporal-based methods, and the hybrid methods, they cannot get rid of the restrictions of the single source (e.g., the same spatial resolution, the same sensor). If the complementary information from the spectral or temporal domain is of a poor quality, the reconstruction effect will be restricted. However, multisource data can bring extraneous useful information from another data source, which does not exist in the sole data source. Concretely, the multisource data from different sensors may be in different resolutions and types (see Fig. 28). Roy et al. [93] touched on this idea to reconstruct the missing information of remote sensing data, and their results showed certain advantages. As we know, the remote sensing data from passive sensors suffer from cloud contamination while the remote sensing data from active sensors get rid of the restrictions of weather conditions. The fusion of these two kinds of data is also worth investigating. Thus, in our opinion, multisource data fusion for missing information reconstruction is another promising direction.

C. High-Efficiency and High-Accuracy Algorithms

Although researchers have proposed all kinds of methods to reconstruct the missing information of remote sensing data, the majority of the high-precision methods are time-consuming. In order to improve the economic benefits, the efficiency should be improved in the future. Furthermore, it should also be required that the algorithm runs fast, on the premise that the accuracy is high enough. In other words, it is a tradeoff problem between the accuracy and efficiency. The ideal situation is that the method has both high accuracy and high efficiency. In the world of big data today, if this tradeoff is able to be settled well, the application potential of remote sensing data will be significantly improved, which is the ultimate goal of missing information reconstruction.

D. Multisource Fusion Task-Oriented Algorithms

Missing information reconstruction is usually the preprocessing step which ensures the accuracy and reliability of the data interpretation. However, different tasks (e.g., classification, change object detection and military quantitative applications) have different requirements. For example, in high-precision public maps, the sensitive military objects are often required to be removed. In this case, low-accuracy and even false reconstruction is allowed, as the result in Fig. 9(e). However, in some quantitative applications, the maintaining of physical attributes may be more important than the satisfaction of visual inspection. For example, phenology applications usually require that the higher NDVI values should be retained in the temporal profile. The task-oriented algorithms have already been discussed in some previous works (e.g., [71], [94]). In order to benefit the practical task of remote sensing data, the task-oriented reconstruction algorithms of missing information should be further designed.

E. Generalization of Missing Information Reconstruction

In this paper, the missing data means that the objective information is completely obscured or not observed. However, there is another kind of missing information for remote sensing data, which can be called partially missing, such as shadow [95], [96], thin cloud [97], and haze [98-100], etc. The partially missing information also greatly affects the application of remote sensing data. Although it is not discussed in this paper, it is a noteworthy aspect for the generalization of missing information reconstruction.

ACKNOWLEDGMENTS

This work was supported by the National Natural Science Foundation of China (NSFC) under Grant Nos. 41271376 and 41422108, the Program for Changjiang Scholars and Innovative Research Team in University under Grant No. IRT1278. The authors would also like to thank the anonymous reviewers and the Guest Editors of this special issue on "Data Fusion in Remote Sensing".

REFERENCES

[1] L. Wang, J. J. Qu, X. Xiong, X. Hao, Y. Xie, and N. Che, "A New Method for Retrieving Band 6 of Aqua MODIS," *IEEE Geoscience and Remote Sensing Letters*, vol. 3, no. 2, pp. 267-270, April, 2006.

[2] C. Zeng, H. Shen, and L. Zhang, "Recovering missing pixels for Landsat ETM+ SLC-off imagery using multi-temporal regression analysis and a regularization method," *Remote Sensing of Environment*, vol. 131, pp. 182-194, April, 2013.

[3] C.-H. Lin, K.-H. Lai, Z.-B. Chen, and J.-Y. Chen, "Patch-Based Information Reconstruction of Cloud-Contaminated Multitemporal Images," *IEEE Transactions on Geoscience and Remote Sensing*, vol. 52, no. 1, pp. 163-174, January, 2014.

[4] F. Melgani, "Contextual reconstruction of cloud-contaminated multitemporal multispectral images," *IEEE Transactions on Geoscience and Remote Sensing*, vol. 44, no. 2, pp. 442-455, February, 2006.

[5] D. Tuia, F. Ratle, F. Pacifici, M. F. Kanevski, and W. J. Emery, "Active Learning Methods for Remote Sensing Image Classification," *IEEE Transactions on Geoscience and Remote Sensing*, vol. 47, no. 7, pp. 2218-2232, July, 2009.

[6] C. Guillemot, and O. Le Meur, "Image Inpainting: Overview and Recent Advances," *IEEE Signal Processing Magazine*, vol. 31, no. 1, pp. 127-144, January, 2014.

[7] M. Bertalmio, G. Sapiro, V. Caselles, and C. Ballester, "Image inpainting," in *the 27th Annual Conference on Computer Graphics and Interactive Techniques (SIGGRAPH)*, 2000, pp. 417-424.

[8] C. Ballester, M. Bertalmio, V. Caselles, G. Sapiro, and J. Verdera, "Filling-in by joint interpolation of vector fields and gray levels," *IEEE Transactions on Image Processing*, vol. 10, no. 8, pp. 1200-1211, August, 2001.

[9] T. F. Chan, and J. Shen, "Nontexture inpainting by curvature-driven diffusions," *Journal of Visual Communication and Image Representation*, vol. 12, no. 4, pp. 436-449, December, 2001.

[10] A. Bugeau, M. Bertalmio, V. Caselles, and G. Sapiro, "A Comprehensive Framework for Image Inpainting," *IEEE Transactions on Image Processing*, vol. 19, no. 10, pp. 2634-2645, October, 2010.

[11] T. Chan, and J. Shen, "Local inpainting models and TV inpainting," *SIAM Journal on Applied Mathematics*, vol. 62, no. 3, pp. 1019-1043, 2001.

[12] C. Zhang, W. Li, and D. Travis, "Gaps-fill of SLC-off Landsat ETM+ satellite image using a geostatistical approach," *International Journal of Remote Sensing*, vol. 28, no. 22, pp. 5103-5122, 2007.

[13] C. Yu, L. Chen, L. Su, M. Fan, and S. Li, "Kriging interpolation method and its application in retrieval of MODIS aerosol optical depth," in *the 19th International Conference on Geoinformatics (ICGI)*, Shanghai, China, 2011, pp. 1-6.

[14] A. Maalouf, P. Carre, B. Augereau, and C. Fernandez-Maloigne, "A Bandelet-Based Inpainting Technique for Clouds Removal From Remotely Sensed Images," *IEEE Transactions on Geoscience and Remote Sensing*, vol. 47, no. 7, pp. 2363-2371, July, 2009.

[15] H. Shen, and L. Zhang, "A MAP-Based Algorithm for Destriping and Inpainting of Remotely Sensed Images," *IEEE Transactions on Geoscience and Remote Sensing*, vol. 47, no. 5, pp. 1492-1502, May, 2009.

[16] H. Shen, Y. Liu, T. Ai, Y. Wang, and B. Wu, "Universal reconstruction method for radiometric quality improvement of remote sensing images," *International Journal of Applied Earth Observation and Geoinformation*, vol. 12, no. 4, pp. 278-286, August, 2010.

[17] Q. Cheng, H. Shen, L. Zhang, and P. Li, "Inpainting for Remotely Sensed Images With a Multichannel Nonlocal Total Variation Model," *IEEE Transactions on Geoscience and Remote Sensing*, vol. 52, no. 1, pp. 175-187, January, 2014.

[18] H. Shen, X. Li, L. Zhang, D. Tao, and C. Zeng, "Compressed Sensing-Based Inpainting of Aqua Moderate Resolution Imaging Spectroradiometer Band 6 Using Adaptive Spectrum-Weighted Sparse Bayesian Dictionary Learning," *IEEE Transactions on Geoscience and Remote Sensing*, vol. 52, no. 2, pp. 894-906, February, 2014.

[19] A. Criminisi, P. Perez, and K. Toyama, "Region filling and object removal by exemplar-based image inpainting," *IEEE Transactions on Image Processing*, vol. 13, no. 9, pp. 1200-1212, September, 2004.

[20] A. A. Efros, and T. K. Leung, "Texture synthesis by non-parametric sampling," in *the 7th IEEE International Conference on Computer Vision (ICCV)*, Kerkyra, Greece, 1999, pp. 1033-1038.

[21] N. Komodakis, "Image Completion Using Global Optimization," in *the 19th IEEE Computer Society Conference on Computer Vision and Pattern Recognition (CVPR)*, New York, USA, 2006, pp. 442-452.

[22] R. Webster, and M. A. Oliver, *Geostatistics for Environmental Scientists*, pp. 271, Chichester: John Wiley & Sons, 2001.

[23] F. Van der Meer, "Remote-sensing image analysis and geostatistics," *International Journal of Remote Sensing*, vol. 33, no. 18, pp. 5644-5676, 2012.

[24] C. Barcelos, and M. A. Batista, "Image inpainting and denoising by nonlinear partial differential equations," in *the 16th Brazilian Symposium on Computer Graphics and Image Processing (SIBGRAPI)*, Sao Carlos, Brazil, 2003, pp. 287-293.

[25] M. M. Oliveira, B. Bowen, R. McKenna, and Y.-S. Chang, "Fast Digital Image Inpainting," in *the International Conference on Visualization, Imaging and Image Processing (VIIP)*, Marbella, Spain, 2001, pp. 261-266.

[26] R. Mendez-Rial, M. Calvino-Cancela, and J. Martin-Herrero, "Anisotropic Inpainting of the Hypercube," *IEEE Geoscience and Remote Sensing Letters*, vol. 9, no. 2, pp. 214-218, March, 2012.

[27] R. C. Hardie, K. J. Barnard, and E. E. Armstrong, "Joint MAP registration and high-resolution image estimation using a sequence of undersampled images," *IEEE Transactions on Image Processing*, vol. 6, no. 12, pp. 1621-1633, December, 1997.

[28] A. N. Tikhonov, and V. Y. Arsenin, *Solutions of ill-posed problems*, New York: Wiley, 1977.

[29] M.-F. Marcos, J.-E. RaulSan, C.-F. Westin, and A.-L. Carlos, "A Novel Gauss-Markov Random Field Approach for Regularization of Diffusion Tensor Maps," *Computer Aided Systems Theory - EUROCAST 2003*, pp. 506-517: Springer Berlin Heidelberg, 2003.

[30] T. Chan, A. Marquina, and P. Mulet, "High-Order Total Variation-Based Image Restoration," *SIAM Journal on Scientific Computing*, vol. 22, no. 2, pp. 503-516, 2000.

[31] Q. Yuan, L. Zhang, and H. Shen, "Hyperspectral Image Denoising Employing a Spectral-spatial Adaptive Total Variation Model," *IEEE Transactions on Geoscience and Remote Sensing*, vol. 50, no. 10, pp. 3660-3677, October, 2012.

[32] A. Buades, B. Coll, and J. M. Morel, "A non-local algorithm for image denoising," in *the 27th IEEE Computer Society Conference on Computer Vision and Pattern Recognition (CVPR)*, San Diego, USA, 2005, pp. 60-65.

[33] K. He, and J. Sun, "Statistics of patch offsets for image completion," in *the 12th European Conference on Computer Vision (ECCV)*, Florence, Italy, 2012, pp. 16-29.

[34] Z. Wang, A. C. Bovik, H. R. Sheikh, and E. P. Simoncelli, "Image quality assessment: from error visibility to structural similarity," *IEEE Transactions on Image Processing*, vol. 13, no. 4, pp. 600-612, April, 2004.

[35] P. Rakwatin, W. Takeuchi, and Y. Yasuoka, "Restoration of Aqua MODIS Band 6 Using Histogram Matching and Local Least Squares Fitting," *IEEE Transactions on Geoscience and Remote Sensing*, vol. 47, no. 2, pp. 613-627, February, 2009.

[36] H. Shen, C. Zeng, and L. Zhang, "Recovering Reflectance of AQUA MODIS Band 6 Based on Within-Class Local Fitting," *IEEE Journal of Selected Topics in Applied Earth Observations and Remote Sensing*, vol. 4, no. 1, pp. 185-192, March, 2011.

[37] I. Gladkova, M. D. Grossberg, F. Shahriar, G. Bonev, and P. Romanov, "Quantitative Restoration for MODIS Band 6 on Aqua," *IEEE Transactions on Geoscience and Remote Sensing*, vol. 50, no. 6, pp. 2409-2416, June, 2012.

[38] X. Li, H. Shen, L. Zhang, H. Zhang, and Q. Yuan, "Dead Pixel Completion of Aqua MODIS Band 6 Using a Robust M-Estimator Multiregression," *IEEE Geoscience and Remote Sensing Letters*, vol. 11, no. 4, pp. 768-772, April, 2014.

[39] J. Zhang, M. K. Clayton, and P. A. Townsend, "Functional Concurrent Linear Regression Model for Spatial Images," *Journal of Agricultural, Biological, and Environmental Statistics,* vol. 16, no. 1, pp. 105-130, March, 2011.

[40] J. Zhang, M. K. Clayton, and P. A. Townsend, "Missing Data and Regression Models for Spatial Images," *IEEE Transactions on Geoscience and Remote Sensing,* vol. 53, no. 3, pp. 1574-1582, March, 2015.

[41] C. Zeng, H. Shen, M. Zhong, L. Zhang, and P. Wu, "Reconstructing MODIS LST Based on Multitemporal Classification and Robust Regression," *IEEE Geoscience and Remote Sensing Letters,* vol. 12, no. 3, pp. 512-516, March, 2015.

[42] X. Zhang, F. Qin, and Y. Qin, "Study on the Thick Cloud Removal Method Based on Multi-Temporal Remote Sensing Images," in *the 1st International Conference on Multimedia Technology (ICMT)*, Malaga, Spain, 2010, pp. 1-3.

[43] S. Benabdelkader, and F. Melgani, "Contextual Spatiospectral Postreconstruction of Cloud-Contaminated Images," *IEEE Geoscience and Remote Sensing Letters,* vol. 5, no. 2, pp. 204-208, April, 2008.

[44] C.-H. Lin, P.-H. Tsai, K.-H. Lai, and J.-Y. Chen, "Cloud Removal From Multitemporal Satellite Images Using Information Cloning," *IEEE Transactions on Geoscience and Remote Sensing,* vol. 51, no. 1, pp. 232-241, January, 2013.

[45] Q. Cheng, H. Shen, L. Zhang, Q. Yuan, and C. Zeng, "Cloud removal for remotely sensed images by similar pixel replacement guided with a spatio-temporal MRF model," *ISPRS Journal of Photogrammetry and Remote Sensing,* vol. 92, pp. 54-68, June, 2014.

[46] B. N. Holben, "Characteristics of maximum-value composite images from temporal AVHRR data," *International Journal of Remote Sensing,* vol. 7, no. 11, pp. 1417-1434, 1986.

[47] J. Inglada, and S. Garrigues, "Land-cover maps from partially cloudy multi-temporal image series: Optimal temporal sampling and cloud removal," in *the 30th IEEE International Geoscience and Remote Sensing Symposium (IGARSS)*, Honolulu, USA, 2010, pp. 3070-3073.

[48] J. Chen, P. Jönsson, M. Tamura, Z. Gu, B. Matsushita, and L. Eklundh, "A simple method for reconstructing a high-quality NDVI time-series data set based on the Savitzky–Golay filter," *Remote Sensing of Environment,* vol. 91, no. 3, pp. 332-344, June, 2004.

[49] P. Jönsson, and L. Eklundh, "TIMESAT-a program for analyzing time-series of satellite sensor data," *Computers & Geosciences,* vol. 30, no. 8, pp. 833-845, October, 2004.

[50] G. J. Roerink, M. Menenti, and W. Verhoef, "Reconstructing cloudfree NDVI composites using Fourier analysis of time series," *International Journal of Remote Sensing,* vol. 21, no. 9, pp. 1911-1917, 2000.

[51] Y. Julien, and J. A. Sobrino, "Comparison of cloud-reconstruction methods for time series of composite NDVI data," *Remote Sensing of Environment,* vol. 114, no. 3, pp. 618-625, March, 2010.

[52] N. Viovy, O. Arino, and A. S. Belward, "The Best Index Slope Extraction (BISE): A method for reducing noise in NDVI time-series," *International Journal of Remote Sensing,* vol. 13, no. 8, pp. 1585-1590, 1992.

[53] M. Ma, and F. Veroustraete, "Reconstructing pathfinder AVHRR land NDVI time-series data for the Northwest of China," *Advances in Space Research,* vol. 37, no. 4, pp. 835-840, 2006.

[54] W. Zhu, Y. Pan, H. He, L. Wang, M. Mou, and J. Liu, "A changing-weight filter method for reconstructing a high-quality NDVI time series to preserve the integrity of vegetation phenology," *IEEE Transactions on Geoscience and Remote Sensing,* vol. 50, no. 4, pp. 1085-1094, April, 2012.

[55] X. Lu, R. Liu, J. Liu, and S. Liang, "Removal of noise by wavelet method to generate high quality temporal data of terrestrial MODIS products," *Photogrammetric Engineering & Remote Sensing,* vol. 73, no. 10, pp. 1129-1139, October, 2007.

[56] P. Jönsson, and L. Eklundh, "Seasonality extraction by function fitting to time-series of satellite sensor data," *IEEE Transactions on Geoscience and Remote Sensing,* vol. 40, no. 8, pp. 1824-1832, August, 2002.

[57] P. S. Beck, C. Atzberger, K. A. Høgda, B. Johansen, and A. K. Skidmore, "Improved monitoring of vegetation dynamics at very high latitudes: A new method using MODIS NDVI," *Remote Sensing of Environment,* vol. 100, no. 3, pp. 321-334, February, 2006.

[58] L. Lorenzi, F. Melgani, and G. Mercier, "Missing-Area Reconstruction in Multispectral Images Under a Compressive Sensing Perspective," *IEEE Transactions on Geoscience and Remote Sensing,* vol. 51, no. 7, pp. 3998-4008, July, 2013.

[59] X. Li, H. Shen, L. Zhang, H. Zhang, Q. Yuan, and G. Yang, "Recovering Quantitative Remote Sensing Products Contaminated by Thick Clouds and Shadows Using Multitemporal Dictionary Learning," *IEEE Transactions on Geoscience and Remote Sensing,* vol. 52, no. 11, pp. 7086-7098, November, 2014.

[60] M. Li, S. C. Liew, and L. K. Kwoh, "Producing cloud free and cloud-shadow free mosaic from cloudy IKONOS images," in *the 23th IEEE International Geoscience and Remote Sensing Symposium (IGARSS)*, Toulouse, France, 2003, pp. 3946-3948.

[61] E. Helmer, and B. Ruefenacht, "Cloud-free satellite image mosaics with regression trees and histogram matching," *Photogrammetric Engineering and Remote Sensing,* vol. 71, no. 9, pp. 1079-1089, September, 2005.

[62] J. Storey, P. Scaramuzza, G. Schmidt, and J. Barsi, "Landsat 7 scan line corrector-off gap filled product development," in *Pecora 16 Conference*, Sioux Falls, USA, 2005, pp. 23-27.

[63] D.-C. Tseng, H.-T. Tseng, and C.-L. Chien, "Automatic cloud removal from multi-temporal SPOT images," *Applied Mathematics and Computation,* vol. 205, no. 2, pp. 584-600, November, 2008.

[64] USGS. "Preliminary Assessment of the Value of Landsat 7 ETM+ Data following Scan Line Corrector Malfunction," May 8, 2010; http://landsat.usgs.gov/documents/SLC_off_Scientific_Usability.pdf.

[65] J. Chen, X. Zhu, J. E. Vogelmann, F. Gao, and S. Jin, "A simple and effective method for filling gaps in Landsat ETM+ SLC-off images," *Remote Sensing of Environment,* vol. 115, no. 4, pp. 1053-1064, April, 2011.

[66] A. Savitzky, and M. J. E. Golay, "Smoothing and differentiation of data by simplified least squares procedures," *Analytical Chemistry,* vol. 36, no. 8, pp. 1627-1639, July, 1964.

[67] C. Song, B. Huang, and S. You, "Comparison of three time-series NDVI reconstruction methods based on TIMESAT," in *the 32th IEEE International Geoscience and Remote Sensing Symposium (IGARSS)*, Munich, Germany, 2012, pp. 2225-2228.

[68] Y. Julien, and J. A. Sobrino, "Global land surface phenology trends from GIMMS database," *International Journal of Remote Sensing,* vol. 30, no. 13, pp. 3495-3513, 2009.

[69] P. J. Sellers, C. J. Tucker, G. J. Collatz, S. O. Los, C. O. Justice, D. A. Dazlich, and D. A. Randall, "A global 1° by 1° NDVI data set for climate studies. Part 2: The generation of global fields of terrestrial biophysical parameters from the NDVI," *International Journal of Remote Sensing,* vol. 15, no. 17, pp. 3519-3545, 1994.

[70] W. Verhoef, M. Menenti, and S. Azzali, "Cover A colour composite of NOAA-AVHRR-NDVI based on time series analysis (1981-1992)," *International Journal of Remote Sensing,* vol. 17, no. 2, pp. 231-235, 1996.

[71] B. A. Latif, R. Lecerf, G. Mercier, and L. Hubert-Moy, "Preprocessing of Low-Resolution Time Series Contaminated by Clouds and Shadows," *IEEE Transactions on Geoscience and Remote Sensing,* vol. 46, no. 7, pp. 2083-2096, July, 2008.

[72] H. Fang, S. Liang, J. R. Townshend, and R. E. Dickinson, "Spatially and temporally continuous LAI data sets based on an integrated filtering method: Examples from North America," *Remote Sensing of Environment,* vol. 112, no. 1, pp. 75-93, January, 2008.

[73] J. Ql, and Y. Kerr, "On current compositing algorithms," *Remote Sensing Reviews,* vol. 15, no. 1-4, pp. 235-256, 1997.

[74] A. Verger, F. Baret, M. Weiss, S. Kandasamy, and E. F. Vermote, "The CACAO Method for Smoothing, Gap Filling, and Characterizing Seasonal Anomalies in Satellite Time Series," *IEEE Transactions on Geoscience and Remote Sensing,* vol. 51, no. 4, pp. 1963-1972, April, 2013.

[75] L. Ke, X. Ding, and C. Song, "Reconstruction of time-series MODIS LST in central Qinghai-Tibet Plateau using geostatistical approach," *IEEE Geoscience and Remote Sensing Letters,* vol. 10, no. 6, pp. 1602-1606, November, 2013.

[76] X. Li, H. Shen, L. Zhang, and H. Li, "Sparse-based reconstruction of missing information in remote sensing images from spectral/temporal complementary information," *ISPRS Journal of Photogrammetry and Remote Sensing,* DOI: 10.1016/j.isprsjprs.2015.03.009.

[77] M. Zhou, H. Chen, J. Paisley, L. Ren, L. Li, Z. Xing, D. Dunson, G. Sapiro, and L. Carin, "Nonparametric Bayesian Dictionary Learning for Analysis of Noisy and Incomplete Images," *IEEE Transactions on Image Processing,* vol. 21, no. 1, pp. 130-144, January, 2012.

[78] X. Li, H. Shen, C. Zeng, and P. Wu, "Restoring Aqua Modis Band 6 By Other Spectral Bands Using Compressed Sensing Theory," in *the 4th*

Workshop on Hyperspectral Image and Signal Processing: Evolution in Remote Sensing (WHISPERS), Shanghai, China, 2012, pp. 1-4.

[79] X. Li, H. Shen, H. Li, and L. Zhang, "Analysis Model Based Recovery of Remote Sensing Data," in *the 34th IEEE International Geoscience and Remote Sensing Symposium (IGARSS)*, Quebec, Canada, 2014, pp. 2491-2494.

[80] M. Elad, and M. Aharon, "Image Denoising Via Sparse and Redundant Representations Over Learned Dictionaries," *IEEE Transactions on Image Processing*, vol. 15, no. 12, pp. 3736-3745, December, 2006.

[81] R. R. Irish, J. L. Barker, S. N. Goward, and T. Arvidson, "Characterization of the Landsat-7 ETM+ automated cloud-cover assessment (ACCA) algorithm," *Photogrammetric Engineering & Remote Sensing*, vol. 72, no. 10, pp. 1179-1188, October, 2006.

[82] M. C. M. Team, S. Ackerman, K. Strabala, P. Menzel, R. Frey, C. Moeller, L. Gumley, B. Baum, C. Schaaf, and G. Riggs, "Discriminating clear-sky from cloud with modis algorithm theoretical basis document (mod35)," *ATBD Ref. ATBD-MOD-06, version*, vol. 4, pp. 115, 1997.

[83] Z. Zhu, and C. E. Woodcock, "Object-based cloud and cloud shadow detection in Landsat imagery," *Remote Sensing of Environment*, vol. 118, pp. 83-94, March, 2012.

[84] B. B. Barnes, and C. Hu, "A Hybrid Cloud Detection Algorithm to Improve MODIS Sea Surface Temperature Data Quality and Coverage Over the Eastern Gulf of Mexico," *IEEE Transactions on Geoscience and Remote Sensing* vol. 51, no. 6, pp. 3273-3285, June, 2013.

[85] P. L. Scaramuzza, M. A. Bouchard, and J. L. Dwyer, "Development of the Landsat Data Continuity Mission Cloud-Cover Assessment Algorithms," *IEEE Transactions on Geoscience and Remote Sensing*, vol. 50, no. 4, pp. 1140-1154, April, 2012.

[86] Z. Zhu, and C. E. Woodcock, "Automated cloud, cloud shadow, and snow detection in multitemporal Landsat data: An algorithm designed specifically for monitoring land cover change," *Remote Sensing of Environment*, vol. 152, pp. 217-234, September, 2014.

[87] C. Latry, C. Panem, and P. Dejean, "Cloud detection with SVM technique," in *IEEE International Geoscience and Remote Sensing Symposium (IGARSS)*, Barcelona, Spain, 2007, pp. 448-451.

[88] B. Huang, H. Zhang, H. Song, J. Wang, and C. Song, "Unified fusion of remote-sensing imagery: generating simultaneously high-resolution synthetic spatial–temporal–spectral earth observations," *Remote Sensing Letters*, vol. 4, no. 6, pp. 561-569, June, 2013.

[89] Y. Gao, H. Xie, T. Yao, and C. Xue, "Integrated assessment on multi-temporal and multi-sensor combinations for reducing cloud obscuration of MODIS snow cover products of the Pacific Northwest USA," *Remote Sensing of Environment*, vol. 114, no. 8, pp. 1662-1675, August, 2010.

[90] L. Zhang, H. Shen, W. Gong, and H. Zhang, "Adjustable Model-Based Fusion Method for Multispectral and Panchromatic Images," *IEEE Transactions on Systems, Man, and Cybernetics, Part B: Cybernetics*, vol. 42, no. 6, pp. 1693-1704, December, 2012.

[91] W. Zhou, and A. C. Bovik, "A universal image quality index," *IEEE Signal Processing Letters*, vol. 9, no. 3, pp. 81-84, March, 2002.

[92] M. J. Pringle, M. Schmidt, and J. S. Muir, "Geostatistical interpolation of SLC-off Landsat ETM+ images," *ISPRS Journal of Photogrammetry and Remote Sensing*, vol. 64, no. 6, pp. 654-664, November, 2009.

[93] D. P. Roy, J. Ju, P. Lewis, C. Schaaf, F. Gao, M. Hansen, and E. Lindquist, "Multi-temporal MODIS–Landsat data fusion for relative radiometric normalization, gap filling, and prediction of Landsat data," *Remote Sensing of Environment*, vol. 112, no. 6, pp. 3112-3130, June, 2008.

[94] R. J. Donohue, T. R. McVicar, and M. L. Roderick, "Climate-related trends in Australian vegetation cover as inferred from satellite observations, 1981–2006," *Global Change Biology*, vol. 15, no. 4, pp. 1025-1039, April, 2009.

[95] L. Lorenzi, F. Melgani, G. Mercier, and Y. Bazi, "Assessing the Reconstructability of Shadow Areas in VHR Images," *IEEE Transactions on Geoscience and Remote Sensing*, vol. 51, no. 5, pp. 2863-2873, May, 2013.

[96] H. Li, L. Zhang, and H. Shen, "An Adaptive Nonlocal Regularized Shadow Removal Method for Aerial Remote Sensing Images," *IEEE Transactions on Geoscience and Remote Sensing*, vol. 52, no. 1, pp. 106-120, January, 2014.

[97] H. Shen, H. Li, Y. Qian, L. Zhang, and Q. Yuan, "An effective thin cloud removal procedure for visible remote sensing images," *ISPRS Journal of Photogrammetry and Remote Sensing*, vol. 96, pp. 224-235, October, 2014.

[98] H. Li, L. Zhang, and H. Shen, "A Principal Component Based Haze Masking Method for Visible Images," *IEEE Geoscience and Remote Sensing Letters*, vol. 11, no. 5, pp. 975-979, May, 2014.

[99] X. Lan, L. Zhang, H. Shen, Q. Yuan, and H. Li, "Single image haze removal considering sensor blur and noise," *EURASIP Journal on Advances in Signal Processing*, vol. 2013, no. 1, pp. 1-13, April, 2013.

[100] H. Li, L. Zhang, H. Shen, and P. Li, "A Variational Gradient-based Fusion Method for Visible and SWIR Imagery," *Photogrammetric Engineering & Remote Sensing*, vol. 78, no. 9, pp. 947-958, September, 2012.

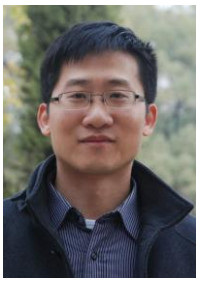

Huanfeng Shen (M'10–SM'13) received the B.S. degree in surveying and mapping engineering and the Ph.D. degree in photogrammetry and remote sensing from Wuhan University, Wuhan, China, in 2002 and 2007, respectively.

In July 2007, he joined the School of Resource and Environmental Sciences, Wuhan University, where he is currently a full professor. His research interests include image quality improvement, remote sensing mapping and application, data fusion and assimilation, regional and global environmental change. Dr. Shen has published more than 100 research papers. He has been supported by several talent programs, such as China National Science Fund for Excellent Young Scholars (2014), the New Century Excellent Talents by the Ministry of Education of China (2011), Hubei Science Fund for Distinguished Young Scholars (2011). He serves as a director of China Association of Remote Sensing Application. He is currently a member of the Editorial Board of JOURNAL OF APPLIED REMOTE SENSING.

Xinghua Li (S'14–) received the B.S. degree in geographical information system from Wuhan University, Wuhan, China, in 2011.

He is currently working toward the Ph.D. degree at the School of Resource and Environmental Sciences, Wuhan University, Wuhan, China. His current research interests focus on missing information reconstruction of remote sensing image, cloud removal of remote sensing image, compressed sensing based image processing and sparse representation.

Qing Cheng received the B.S. degree in the geographic information system from Wuhan University, Wuhan, China, in 2010, where she is currently working toward the Ph.D. degree in the State Key Laboratory of Information Engineering in Surveying, Mapping and Remote Sensing.

Her research interests include image restoration, inpainting, and remote sensing image enhancement.

Chao Zeng received the B.S. degree in Resources-Environment and Urban-Rural Planning Management, the M.S. degree in surveying and mapping engineering and the Ph.D. degree in photogrammetry and remote sensing from Wuhan University, Wuhan, China, in 2009, 2011 and 2014, respectively.

Currently he is a postdoctoral researcher in the Department of Hydraulic Engineering, Tsinghua University, Beijing, China. His current research interests focus on remote sensing image processing and remote sensing applications.

Gang Yang received the M.S. degree in geographical information system from Hunan University of Science and Technology, Xiangtan, China, in 2012.

He is currently working toward the Ph.D. degree at the School of Resource and Environmental Sciences, Wuhan University, Wuhan, China. His current research interests focus on image inpainting, and remote sensing time-series products temporal reconstruction.

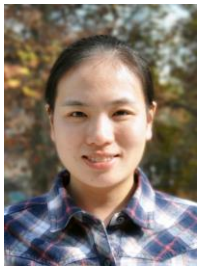

Huifang Li (M'14–) received the B.S. degree in geographical information science from China University of Mining and Technology, Xuzhou, in 2008, and the Ph. D degree in photogrammetry and remote sensing from Wuhan University, Wuhan, in 2013.

She is currently working in School of Resource and Environmental Sciences as a lecturer, Wuhan University, China. Her research interests include variational methods, dehazing and deshadowing of remote sensing images.

Liangpei Zhang (M'06–SM'08) received the B.S. degree in physics from Hunan Normal University, ChangSha, China, in 1982, the M.S. degree in optics from the Xi'an Institute of Optics and Precision Mechanics of Chinese Academy of Sciences, Xi'an, China, in 1988, and the Ph.D. degree in Photogrammetry and Remote Sensing from Wuhan University, Wuhan, China, in 1998.

He is currently the Head of the Remote Sensing Division, State Key Laboratory of Information Engineering in Surveying, Mapping and Remote Sensing, Wuhan University. He is also a Chang-Jiang Scholar Chair Professor appointed by the Ministry of Education of China. He is currently a Principal Scientist for the China State Key Basic Research Project (20112016) appointed by the Ministry of National Science and Technology of China to lead the remote sensing program in China. He has more than 410 research papers. He is the holder of 15 patents. He has won the 2010 the best paper Boeing award and 2013 best paper ERDAS award of American Society of Photogrammetry and Remote Sensing (ASPRS), respectively His research interests include hyperspectral remote sensing, high-resolution remote sensing, image processing, and artificial intelligence.

Dr. Zhang is a Fellow of the Institution of Engineering and Technology, an Executive Member (Board of Governor) of the China National Committee of the International Geosphere-Biosphere Programme, and an Executive Member of the China Society of Image and Graphics. He regularly serves as a Co-chair of the series SPIE Conferences on Multispectral Image Processing and Pattern Recognition, Conference on Asia Remote Sensing, and many other conferences. He edits several conference proceedings, issues, and Geoinformatics symposiums. He also serves as an Associate Editor of the International Journal of Ambient Computing and Intelligence, the International Journal of Image and Graphics, the International Journal of Digital Multimedia Broadcasting, the Journal of Geo-spatial Information Science, the Journal of Remote Sensing, and the IEEE TRANSACTIONS ON GEOSCIENCE AND REMOTE SENSING.